

Review

Mechanistic Insights into WO₃ Sensing and Related Perspectives

Mauro Epifani 

Istituto per la Microelettronica e i Microsistemi, IMM-CNR, Via Monteroni, 73100 Lecce, Italy; maurosalvatore.epifani@cnr.it

Abstract: Tungsten trioxide (WO₃) is taking on an increasing level of importance as an active material for chemoresistive sensors. However, many different issues have to be considered when trying to understand the sensing properties of WO₃ in order to rationally design sensing devices. In this review, several key points are critically summarized. After a quick review of the sensing results, showing the most timely trends, the complex system of crystallographic WO₃ phase transitions is considered, with reference to the phases possibly involved in gas sensing. Appropriate attention is given to related investigations of first principles, since they have been shown to be a solid support for understanding the physical properties of crucially important systems. Then, the surface properties of WO₃ are considered from both an experimental and first principles point of view, with reference to the paramount importance of oxygen vacancies. Finally, the few investigations of the sensing mechanisms of WO₃ are discussed, showing a promising convergence between the proposed hypotheses and several experimental and theoretical studies presented in the previous sections.

Keywords: WO₃; chemoresistive sensors; sensing mechanisms; oxygen vacancies



Citation: Epifani, M. Mechanistic Insights into WO₃ Sensing and Related Perspectives. *Sensors* **2022**, *22*, 2247. <https://doi.org/10.3390/s22062247>

Academic Editor: Chris Blackman

Received: 14 February 2022

Accepted: 11 March 2022

Published: 14 March 2022

Publisher's Note: MDPI stays neutral with regard to jurisdictional claims in published maps and institutional affiliations.



Copyright: © 2022 by the author. Licensee MDPI, Basel, Switzerland. This article is an open access article distributed under the terms and conditions of the Creative Commons Attribution (CC BY) license (<https://creativecommons.org/licenses/by/4.0/>).

1. Introduction

Tungsten trioxide (WO₃) is currently attracting increasing attention as a material spanning several applications. Progress has been recently reviewed [1] on the electrochromic properties of WO₃, one of the early notable features of this material [2]. The photochromic properties of WO₃ have also been recently reviewed [3]. Throughout the years, other fields of interest have emerged, such as solar hydrogen generation [4,5], the photoelectrochemical [6,7] and photocatalytic [8–10] properties of WO₃, water remediation [11–13] and energy storage [14,15]. Along with these recently emerging applications, the field of gas sensing was one of the earliest applications of WO₃ together with electrochromic devices. While one the earliest reports on chemoresistive sensing with WO₃ dates back to 1967 [16], interest in developing WO₃-based sensors has since then steadily increased through early applications to H₂S [17,18]. Currently, full reviews are devoted to the topic [19–22] (while of remarkable interest, WO₃ sensors based on a gasochromic effect [23] will not be considered in the present work). On the one hand, the perusal of these reviews allows for the confirmation that a plethora of target analytes have been tested. On the other hand, a coherent picture of the factors governing sensing behavior has not yet emerged. In particular, the understanding of the sensing properties of WO₃ is mainly based on the widely accepted concept of the modulation of the surface charge depletion layer [24] by the surface-adsorbed gaseous species. However, without a more detailed understanding of how and where the gaseous analytes react with the sensor surface, the depletion layer is more of a working hypothesis than an articulated model. Therefore, it seemed appropriate to devote a review work to the principles and issues related to WO₃-based sensing to serve as an operative reference about the established facts, the known issues and possible further development pathways. This work is structured as follows. First, a succinct summary of some interesting results on WO₃-based sensing will be presented. Then, the interconnection between structure, surface and surface defects in WO₃, with particular reference to oxygen vacancies, will be discussed, as these are closely connected to the gas-sensing field. This discussion will be

carried out by referring to both experimental findings and first principles studies. Finally, the few recent mechanistic studies on WO_3 sensors will be discussed, showing that a fruitful convergence is appearing among fundamental studies of WO_3 surfaces and the material's gas-sensing properties. As a notice to the reader, noble metal loaded WO_3 sensors are not the focus of the present review, despite the fact that several interesting results can be found in the literature [25]. Analogously, sensing [26,27] based on hexagonal [28–30] WO_3 is a very timely topic but will not be covered in the present work. The reason is that such topics are, relatively speaking, in their infancy compared to pure WO_3 in “conventional” phases.

2. Sensing Capabilities of WO_3

WO_3 is the second most studied gas-sensing material after SnO_2 [31], and therefore it is not surprising that a large range of analytes have been tested for WO_3 -based detection. However, some general trends have been emerging, highlighting WO_3 as a powerful sensor of NO_2 and acetone in particular. Therefore, these two gases will be considered in more detail in the present section in order to evidence the physico-chemical properties of WO_3 which are relevant for gas sensing. An additional paragraph will be devoted to the sensing of NH_3 and amines, where WO_3 seems in general to perform less well than in the case of the other two gases.

2.1. NO_2

Most probably, the first study of WO_3 as an NO_2 sensor was published in 1991 by Yamazoe and coworkers [32]. The authors obtained a response of 97 at 300 °C to 80 ppm NO_2 . It was not possible to decrease the operating temperature due to exceedingly high electrical resistance attained below 300 °C. However, the obtained data allowed the authors to hypothesize that NO_2 adsorption was responsible for the sensor response. We shall see in Section 4 that the most recent studies point to a reaction of NO_2 with the surface oxygen vacancies. In a following paper, the authors evidenced the grain size effect on the device response [33]. Since then, materials research has focused on various features of the WO_3 sensing layer. An important trend is the use of lamellar materials. Yamazoe and coworkers prepared WO_3 lamellae [34] by acidification of Na_2WO_4 and found a response larger than 150 at 200 °C to 500 ppb NO_2 . Later on, Lee et al. [35] reported a response of about 960 to 5 ppm NO_2 at 200 °C. The interest in such a morphology has not decreased through the years. For instance, Wang et al. [36] reported a response of almost 6 to 50 ppb NO_2 at 140 °C. More recently, Wang et al. reported a response larger than 450 to 10 ppm NO_2 at 100 °C [37]. The importance of having largely accessible surfaces was evidenced by Lee et al. [38], who used multi-shelled WO_3 spheres to detect down to 50 ppb NO_2 at 100 °C, with a response of about 100. It is clear from a more in-depth analysis of the literature, one which is reported in the following passages, that there is an interest in controlling the morphology of WO_3 and obtaining high surface area structures.

You et al. [39] prepared monoclinic WO_3 nanosheets assembled in microspheres by acid etching of CaWO_4 hollow microspheres. They obtained a response of about 50 to 100 ppb NO_2 at 75 °C. Akamatsu et al. [40] prepared monoclinic WO_3 nanoplatelets assembled in microspheres by a surfactant-aided polyol process. A response of about 80 was obtained to 1 ppm NO_2 at 200 °C. An et al. [41] reported an interesting monoclinic WO_3 nanotube morphology prepared by TeO_2 templating. A response of about 7 at 300 °C to 5 ppm NO_2 was reported. Qi et al. [42] prepared monoclinic WO_3 nanocolumns by a surfactant-free hydrothermal process. They reported the best operating temperature to be 110 °C, with a response of about 22 to 10 ppm NO_2 . Wang et al. [43] prepared monoclinic WO_3 flower-like nanostructures by a surfactant-free solvothermal method. They obtained a response larger than 30 at 100 °C to 50 ppb NO_2 . Khan et al. [44] prepared monoclinic WO_3 nanosheets by sonicating W powders in nitric acid, and could detect down to 40 ppb NO_2 at 150 °C, with a response of 30. Harale et al. [45] prepared monoclinic WO_3 nanobricks by the oxidation of metallic tungsten in H_2O_2 . The resulting solution was used for the direct growth of the nanobricks onto glass substrates in autoclave conditions. The maximum

response to 100 ppm NO₂ was about 12, which, specifically, was obtained at 300 °C, while at lower temperatures a lower response was measured. Hua et al. [46] prepared monoclinic WO₃ nanosheets by the acidification of Na₂WO₄. The thickness of the nanosheets was about 10 nm, much less than the width of the depletion layer in clean air conditions [33]. The authors supposed NO₂ adsorption to be the basis of the sensing mechanism, and attributed the nonlinear behavior of the response at low NO₂ concentrations (below 2 ppm) to competition with oxygen adsorption. A response of more than 32 was obtained at 300 °C to 4 ppm NO₂. Beknalkar et al. [47] prepared 3D monoclinic WO₃ nanoflowers and obtained a response larger than 50 to 100 ppm NO₂ at 100 °C. Interestingly, Song et al. [48] observed that triclinic WO₃ nanosheets prepared via the hydrothermal method displayed a larger response to NO₂ than monoclinic and hexagonal WO₃. They reported a response of 18.8 to 300 ppb of NO₂ at 100 °C. Morais et al. [49] prepared monoclinic WO₃ nanofibers by electrospinning and reported a response larger than four orders of magnitude to 50 ppm of NO₂ at 150 °C.

Without detailing the results of an exceedingly long list of papers, we can notice some essential features with the help of Table 1. First of all, almost all the references report the formation of monoclinic WO₃ after the heat-treatments necessary for thermally stabilizing the samples. Secondly, almost all the works report decreasing responses with increasing operating temperatures, supporting Yamazoe's early model. Third, the influence of a porous accessible structure (lamellae, porous spheres, etc.) clearly emerges. The fourth point is that the authors of several papers increasingly indicate the importance of oxygen vacancies in determining the WO₃ response to NO₂ [50]. We will return to this last observation for a more in-depth discussion in the following passages. For now, we will proceed by perusing some relevant literature on acetone sensing.

Table 1. Summary of the main features of the WO₃-based NO₂ sensors described in Section 2.1.

Sample Morphology	Phase Composition	Gas Concentration	Response	Operating Temperature (°C)	Reference
Sintered powder	n/d	80 ppm	97	300	[32]
Lamellae	Monoclinic	500 ppb	>150	200	[34]
Nanoplates	Monoclinic	5 ppm	960	200	[35]
2D nanosheets	Monoclinic	50 ppb	~6	140	[36]
Porous nanosheets	Monoclinic	10 ppm	>450	100	[37]
Yolk-shell spheres	Monoclinic	50 ppb	~100	100	[38]
Nanosheets	Monoclinic	100 ppb	~50	75	[39]
Nanoplatelets	Monoclinic	1 ppm	~80	200	[40]
Nanotubes	Monoclinic	5 ppm	7	300	[41]
Nanoflowers	Monoclinic	50 ppb	>30	100	[43]
Nanocolumns	Monoclinic	10 ppm	22	110	[42]
Nanosheets	Monoclinic	40 ppb	30	150	[44]
Nanobricks	Monoclinic	100 ppm	12	300	[45]
Nanosheets	Monoclinic	4 ppm	>32	300	[46]
Nanoflowers	Monoclinic	100 ppm	>50	100	[47]
Nanosheets	Triclinic	300 ppb	18.8	100	[48]
Nanofibers	Monoclinic	50 ppm	>10 ⁴	150	[49]

2.2. Acetone

WO₃ acetone sensors have been attracting special attention in the context of applications related to breath analysis [31,51,52], where humidity-independent acetone sensors

are important for the monitoring of diabetes. However, WO₃-based acetone sensing has a long history. In 2004 [53], Li and coworkers operated WO₃ hollow spheres-based devices at 400 °C to detect 50 ppm of acetone with a response of about 3.5. In 2007, Khadayate et al. [54] used triclinic WO₃ thick films for obtaining a response of 4.56 at 300 °C to 50 ppm acetone. In 2011, Chen et al. [55] used WO₃ nanoplates to detect down to 2 ppm of acetone (a response of about 5) at 300 °C. Shi et al. [56] used monoclinic WO₃ nanocrystals at 350 °C to get a response of 10 to acetone at a concentration of 10 ppm. Similarly to NO₂, the interest in such morphologies has steadily increased, to the degree that, in 2012, Liu et al. [57] found 307 °C as the best operating temperature for WO₃ nanoplates for detecting 300 ppm acetone, with a response of almost 50. In the same year, Chen and coworkers [58] used WO₃ nanoplates with uneven surfaces to detect acetone at 200 °C (the response was about 40 to 500 ppm). Wang et al. [59] used nanoflowers composed of WO₃ nanorods to detect 100 ppm of acetone at 300 °C (the response was 7). The interest in different morphologies has extended to nanotube-based devices, which could provide a response of 42.5 to 100 ppm acetone at 250 °C [60].

Chen et al. [61] used a hydrothermal process to prepare monoclinic urchin-like, rod-like and plate-like WO₃. With urchin-like structures, they obtained a response of almost 15 to 25 ppm acetone at 300 °C. Zhang et al. [62] employed a hydrothermal process in varying acid conditions to prepare various crystallographic phases of WO₃. However, after heat-treatment at 450 °C, monoclinic WO₃ nanoplates were obtained. At an operating temperature of 300 °C, a response of about 8 to 100 ppm acetone was reported. A facet-dependent response was evidenced by Yin et al. [63], who reported a response of almost 50 to 100 ppm acetone at 340 °C, evidencing that the minimum nanoplate thickness was associated with the largest gas response among all the synthesized materials. Jia et al. [64] observed that triclinic WO₃ nanosheets were more selective than monoclinic nanosheets, and detected 1 ppm of acetone at 230 °C with a response of 2.04. Xu et al. [65] demonstrated that monoclinic WO₃ mesoporous nanofibers can be used to detect 50 ppm of acetone at 300 °C, with a response of 22, which is an improved result with respect to non-porous samples. Chang et al. [66] prepared WO₃ nanosheets via the oxidation of WS₂ nanostructures, and could detect 50 ppm acetone at 300 °C, with a response of about 15. As a final recent example, it is worth mentioning the work by Wang et al. [67], where sea-urchin-like monoclinic WO₃ nanostructures were prepared using a hydrothermal method. A response of almost 30 to 100 ppm of acetone at 200 °C was reported.

From the analysis of these examples, whose features are summarized in Table 2, some trends emerge, as in the case of NO₂. As expected, high operating temperatures are needed, typically ranging about 300 °C. There is a remarkably narrow range of responses for similar gas concentrations, which this indicates that acetone sensing is governed by the common features of the employed WO₃ materials and does not depend on the synthesis process. Therefore, ubiquitous defects such as oxygen vacancies can be reasonably suspected to have a crucial effect on sensing properties.

Table 2. Summary of the main features of the WO₃-based acetone sensors described in Section 2.2.

Sample Morphology	Phase Composition	Gas Concentration (ppm)	Response	Operating Temperature (°C)	Reference
Hollow spheres	Monoclinic	50	3.5	400	[53]
Thick films	Triclinic	50	4.56	300	[54]
Nanoplates	Triclinic	2	5	300	[55]
Nanoparticles	Monoclinic	10	10	350	[56]
Nanoplates	Monoclinic	300	50	307	[57]
Nanoplates	Monoclinic	500	40	200	[58]

Table 2. Cont.

Sample Morphology	Phase Composition	Gas Concentration (ppm)	Response	Operating Temperature (°C)	Reference
Flower-like	Monoclinic	100	7	300	[59]
Nanotubes	Monoclinic	100	42.5	250	[60]
Urchin-like	Monoclinic	25	15	300	[61]
Nanoplates	Monoclinic	100	8	300	[62]
Nanosheets	Monoclinic	100	50	340	[63]
Nanosheets	Triclinic	1	2.04	230	[64]
Mesoporous nanofibers	Monoclinic	50	22	300	[65]
Nanosheets	Monoclinic	50	15	300	[66]
Urchin-like	Monoclinic	100	30	200	[67]

2.3. Ammonia and Related Gases

While NO₂ and acetone sensing applications span a large part of WO₃-related publications, it is of interest to peruse the much less numerous applications devoted to ammonia and amines, since the detection of such gases may shed light on the adsorption properties of WO₃.

In 1992, Yamazoe and coworkers [68] already investigated the ammonia-sensing properties of WO₃. Au was needed for improving the response; the authors noted that the pure material had a response less than five to 50 ppm NH₃ in the entire operation temperature range (200–600 °C). This limited response, and the need of additives such as Cr, was confirmed by Jimenez et al. [69,70]. Later on, similar a response (5–6) to 50 ppm of ammonia was noted at about 250 °C [71]. Nguyen et al. [72] synthesized monoclinic WO₃ nanowires and reported a maximum response of 9.7 to 1500 ppm NH₃ at 250 °C. Therefore, a clear convergence can be observed among various papers, where the materials were prepared by different techniques (even orthorhombic WO₃ nanofibers prepared by electrospinning were also studied, with similar results [73]), which report a limited response to ammonia. Such poor responses, and the consequent need of additives such as Cr [74], also helps to explain why WO₃ has been seldom considered for ammonia sensing. Even more recent results with other material typologies, such as nanosheets assemblies [75] and nanoplates [76], are in line with the early papers. Despite the limited number of publications about the topic, the role of the surface sites occupied by additives [69] and the concentration of oxygen vacancies [74] has clearly emerged.

Ammonia related compounds, such as simple alkylamines, have been more efficiently detected than ammonia itself. What is likely the first report of trimethylamine (TMA) sensing below a concentration of 100 ppm concerned the use of WO₃ hollow spheres: Lee et al. [77] could detect 5 ppm with a response of 56.9 at about 450 °C. Zhai et al. [78] used WO₃ nanosheets self-assembled into microspheres to detect 50 ppm of triethylamine (TEA) at 220 °C, with a response of almost 16. Even Han et al. [79] reported low temperature TEA detection (150 °C) (a response of 35.3 to 10 ppm) using hierarchical WO₃ spheres. Hu et al. [80] synthesized needle-shaped nanorods and reported optimum TEA sensing at 250 °C, with a response of about 50 to 50 ppm.

The summary in Table 3 shows that there is a rather relevant difference between the NO₂/acetone couple and other analytes, such as ammonia and amines, with the latter providing much lower responses. This behavior suggests the presence of specific features in the surface of WO₃ which make it more amenable to the adsorption of given gases. We are then prompted to have a closer look at WO₃ surfaces and the related crystal structures.

Table 3. Summary of the main features of the WO₃-based ammonia and amines sensors described in Section 2.3.

Sample Morphology	Phase Composition	Gas Concentration (ppm)	Response	Operating Temperature (°C)	Reference
AMMONIA					
Sintered powders	Probably monoclinic	50	<5	200–600	[68]
Nanopowders	Monoclinic + triclinic	500	<5	350	[69]
Nanopowders	Monoclinic + triclinic	50	<6	250	[71]
Nanowires	Monoclinic	1500	9.7	250	[72]
Nanofibers	Orthorhombic	100	<5	300	[73]
Nanosheets	Hexagonal	100	35	350	[75]
Nanoplates	Monoclinic	100	<20	300	[76]
ALKYLAMINES (TEA/TMA)					
Hollow spheres	Orthorhombic	5	56.9	450	[77]
Nanosheets assembled in microspheres	Monoclinic	50	16	220	[78]
Hierarchical spheres	Monoclinic	10	35.3	150	[79]
Nanorods	Monoclinic	50	50	250	[80]

3. WO₃ Structures and Surfaces

3.1. Structural Complexity of WO₃ and Relevant Hints for the Field of Gas-Sensing

Saying “WO₃” only is rather a generic reference. A complex system of phase equilibria is associated with the composition of simple trioxide [81–83]. Upon heating from a low temperature (up to −50 °C), phase transitions are reported, such as the transition from a monoclinic (ϵ -WO₃) phase [84–86] to a triclinic (δ -WO₃) one [83,87–89], and up to 17 °C, this is followed by another monoclinic phase (γ -WO₃) [89–91]. An orthorhombic phase is found from 327 °C (β -WO₃) [92,93] and is followed, from 740 °C, by a tetragonal phase (α -WO₃) [92,94]. A visual summary of these phase transitions is given in Figure 1.

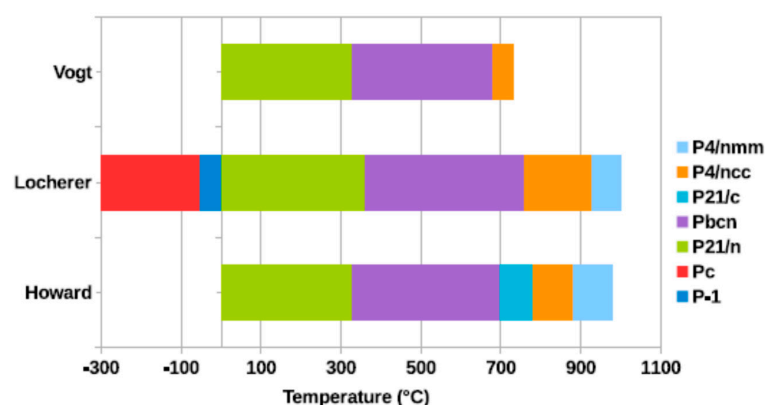


Figure 1. A visual summary of the crystallographic phase transitions in WO₃, as obtained from the data published by the indicated authors. Reprinted with permission from [81]: H. Hamdi, E. K. H. Salje, P. Ghosez and E. Bousquet, Phys. Rev. B 94, 245124, 2016. Copyright (2016) The American Physical Society. License Number RNP/21/DEC/047874.

A brief account of the historical development of structural investigations into WO₃ has been provided by Howard et al. [95]. There are other phase transitions, but these are not discussed here for the sake of brevity, since they are observed at high temperatures (the interested reader can refer to the detailed description and references in ref. [96]). The

reason for the complex structural behavior of WO_3 can be understood if it is considered that WO_3 possesses the ReO_3 structure, where metal cations occupy the center of the oxygen octahedra sharing the corners. However, with respect to ReO_3 (and to the perovskite structure from which both ReO_3 and WO_3 can be derived via removal of the A cation from the general ABO_3 formula), WO_3 features a whole set of possible distortions concerning both the octahedra relative positions (tilting) and the W cation position. In particular, as shown by Woodward et al. [83], the γ and δ phases are differentiated by the in-phase or out-of-phase tilting of the octahedra, respectively, as depicted in Figure 2. This close relationship between the two phases may partially explain their possible simultaneous presence in WO_3 samples. It is interesting to note that ReO_3 displays metallic conductivity, while intrinsic WO_3 is an insulator (however, n-type conductivity is usually reported due to systematic oxygen non-stoichiometry [97]). In one of the earliest works devoted to the modeling of WO_3 , Stachiotti et al. [98] contributed to the explanation for differences between ReO_3 and the hypothetical cubic structure of WO_3 , referring to the stability of the cubic structure upon lattice deformations. The translation of a metal cation along a lattice direction generates the hybridization of the O 2p and Re (d/t_{2g}) orbitals (onset of π bonding between O and W), resulting in a level with a bonding contribution to the valence band and a level with an antibonding contribution to the conduction band. The latter would be occupied in ReO_3 , which is opposed to lattice distortion, so ReO_3 is cubic. In WO_3 , such a level is empty and the structure distortion is stable. Since the removal of the A cation from the perovskite structure leaves an empty space at the center of the octahedron, foreign cations can be accommodated, giving rise to tungsten bronzes [99] (such as NaWO_3). The latter also have an extra electron with respect to WO_3 , provided by the additional cation, and therefore they remain cubic, like ReO_3 , and are highly conductive. The cubic structure of WO_3 was considered in ref. [98], analogously to earlier studies [100,101], for reasons connected to computational feasibility. However, cubic WO_3 is not a stable phase due to the distortions described above, which are energetically preferred to cubic symmetry (such distortions are, in turn, a case of pseudo Jahn–Teller distortion [102]).

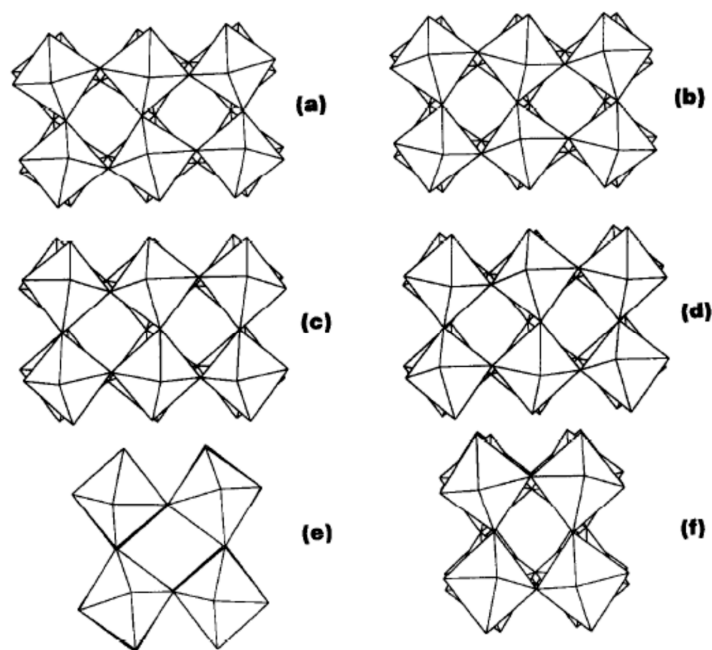


Figure 2. Tilt patterns of WO_3 : (a) monoclinic (001) projection, x -axis vertical; (b) triclinic (001) projection, x -axis vertical; (c) monoclinic (100) projection, z -axis vertical; (d) triclinic (100) projection, z -axis vertical; (e) monoclinic (010) projection, z -axis vertical; (f) triclinic (010) projection, z -axis vertical. Figure and caption reprinted from ref. [83]: J. Phys. Chem. Solids, Vol. 56, No. 10. P. M. Woodward, A. W. Sleight and T. Vogts, Structure Refinement Of Triclinic Tungsten Trioxide, pp. 1305–1315, copyright (1995) with permission from Elsevier. License number: 5223660238738.

For this reason, increasing computational capabilities have prompted renewed interest in modelling the structure of WO_3 . De Wijs et al. [103] used a DFT (Density Functional Theory) methodology in the context of Generalized Gradient Approximation (GGA) for modelling several WO_3 polymorphs. They confirmed that lattice distortions play a paramount role in determining the electronic structure of WO_3 phases. In particular, the splitting of the W-O distances along different crystal axes is a fundamental phenomenological parameter that clearly evidences newly occurring electronic interactions. For instance, the simple modification from a cubic to a tetragonal structure involves alternate short and long W-O bonds along the z axis. The newly appearing overlapping of some of the W and O orbitals results in a bonding–antibonding interaction, with a strong influence on the valence and conduction bands. In the structures that are of major interest for sensors, i.e., the δ and γ phases, a similar phenomenon occurs, but this involves a splitting of the bond lengths along all the crystal axes. Wang et al. [104] used a hybrid functional to improve the estimation of the bandgap of WO_3 polymorphs. Later on, Hamdi et al. [81] used a different hybrid functional in the context of DFT modelling to investigate the WO_3 phase diagram and to understand the origin of the various phases on a microscopic scale. After ensuring that the calculated structural parameters agreed with previous studies, the next step was the modelling of the phonon spectra of the WO_3 polymorphs. The authors demonstrated that the instability branches in the phonon spectra of cubic WO_3 could be removed by the condensation of various modes of the cubic phase, and the newly arising phonon spectra were in very good agreement with the experimental polymorphs of WO_3 .

Even when only referring to these early considerations and studies, it should be made clear that properly considering the structures and defects of WO_3 is a delicate and important task.

From this knowledge about WO_3 structures, some operative considerations can be drawn that are of specific interest for the field of gas-sensing. First of all, monoclinic–orthorhombic transition occurs just above 300 °C. Therefore, any understanding of the sensing properties of WO_3 cannot disregard the operating temperature of the device and the possibility that a different phase might be formed at the highest operating temperatures. There has recently been an experimental investigation of this issue, and this will be discussed in the final section. The second point concerns the very likely co-existence of δ and γ phases in the as-prepared samples.

As described in detail by Woodward et al. [83], the boundary between the two phases is not sharp; while the transition from the triclinic δ phase to the monoclinic γ phase is generally accepted to occur at 17 °C, the triclinic form seems to be the most stable one at room temperature, where it is indefinitely stable, while the monoclinic phase is converted to the triclinic upon grinding at 25 °C. In practice, it cannot be excluded that a mixture of the two phases is present in the prepared samples after cooling to room temperature [105–107]. In principle, the two phases can be distinguished by X-ray diffraction. However, as observed by Jimenez et al. [108], the envelope of reflections to be used for discriminating the phases, placed at a 2Θ value of about 34° , may fail to provide a clear response due to instances of peak broadening in the case of nanocrystalline samples. The authors employed a method proposed by Cazzanelli et al. [106] (this reference also quotes an earlier paper where the different Raman spectra between the two phases was reported) based on Raman spectroscopy, since the monoclinic phase displayed a band at 34 cm^{-1} , while, for the triclinic one, the band was at 43 cm^{-1} . In Figure 3, the clearly-distinguished Raman spectra for the two phases are shown, as originally reported in ref. [106].

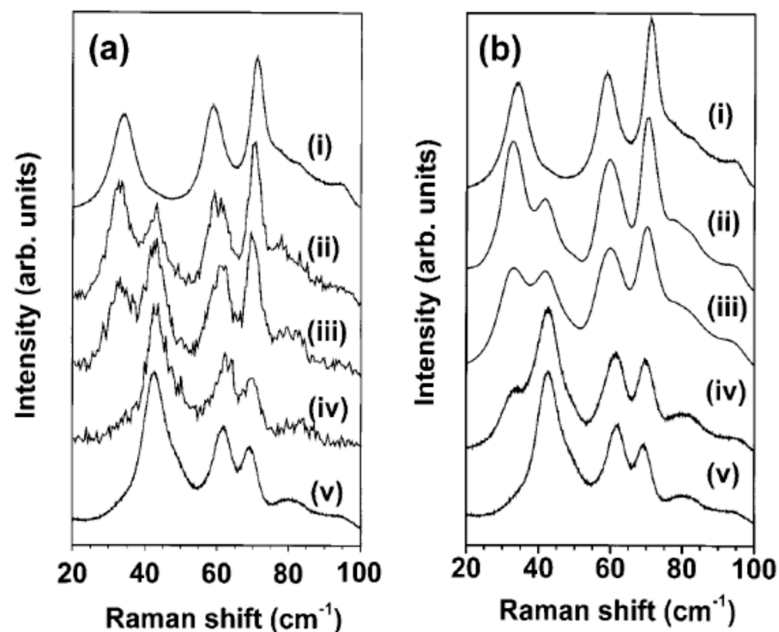


Figure 3. (a) Raman spectra of WO_3 powder samples that were mechanically pressed for various time periods: (i) starting virgin powder (γ -phase); (ii) after 5 s compression; (iii) after 10 s compression; (iv) after 120 s compression; (v) reference treated powder sample, after 10 min moderate milling (δ -phase). Note the strong rearrangement of the low-frequency spectra after the early steps of pressure application. (b) Low-frequency Raman spectra collected at RT on WO_3 virgin powder rapidly cooled by immersion in liquid nitrogen and kept there for different time periods: (i) starting virgin powder; (ii) after 5 s immersion in LN_2 ; (iii) 1 min immersion; (iv) 10 min immersion; (v) 2 h immersion. The varying intensity ratio between the peaks at 34 and 43 cm^{-1} is clearly visible. Reprinted from ref. [106]: J. Solid State Chem., Vol. 143, E. Cazzanelli, C. Vinegoni, G. Mariotto, A. Kuzmin, and J. Purans, “Low-Temperature Polymorphism in Tungsten Trioxide Powders and Its Dependence on Mechanical Treatments”, pp. 24–32, Copyright (1999) with permission from Elsevier. License number: 5225870445333.

These considerations should have clarified that the determination of the structure of WO_3 is a delicate issue. Neglecting the complex phase transitions system may result in an inexact starting point for understanding the material’s sensing properties. This issue is even more relevant, currently, due to the above-mentioned interest in faceted materials whose final morphology clearly depends on the crystallographic phase. In turn, the exposed facets also impose which are the most relevant surface defects (e.g., which kind of oxygen vacancies) to be considered in the gas sensing phenomenon. Therefore, the next step of the present discussion will be devoted to the accumulated knowledge on the surface and defects of WO_3 depending on the crystallographic phase.

3.2. Oxygen Vacancies in WO_3

3.2.1. Experimental Findings: Surface Oxygen Vacancies

Electrical Properties

The importance of oxygen vacancies for the electrical properties of WO_3 has been known for long time. In as early as 1970, Berak and Sienko [97] reported an increase in the carrier concentration upon oxygen removal from the triclinic/monoclinic phases in WO_3 single crystals. The dependence of the electrical properties of WO_3 on oxygen stoichiometry has been a steadily recurring observation throughout the years. For instance, Kaneko et al. [109] reported that the resistivity of sputtered WO_3 thin films remarkably depended on the oxygen concentration in the sputtering atmosphere. A critical oxygen concentration of 4–5% was reported, beyond which transparent films were obtained. The resistivity of

the films increased by several orders of magnitude with respect to a sputtering atmosphere with a slightly lower oxygen concentration. Gillet et al. [110] attributed to oxygen vacancies the conductivity of sputtered WO_3 thin films, on the basis of resistivity measurements carried out in different oxygen concentrations. Interestingly, they argued that the observed decrease in conductance activation energy with a decrease in oxygen partial pressure was due to the overlap of increasingly dense defect states, finally resulting in an energy band in the WO_3 gap. Its width, which increased with increasing defect concentrations, would finally result in the disappearance of the gap. Li et al. [111] prepared $\gamma\text{-WO}_3$ films via spray processing and investigated the effect of the annealing atmosphere on the electrical conductance. They, too, observed a conductance increase upon annealing in N_2 and a decrease upon annealing in 95% N_2 -5% O_2 , which were attributed to generation and the healing of oxygen vacancies, respectively. It was only after annealing at temperatures higher than 600 °C that additional conduction mechanisms were supposed.

Spectroscopic Studies

Early evidence was obtained by X-ray photoelectron spectroscopy (XPS) of the existence of several W oxidation states in WO_3 in the context of the electrochromism of amorphous WO_3 thin films. It is worth providing a brief historical sketch of the development of the spectral interpretation. Hollinger et al. [112] observed an additional signal in the valence band spectra of UV irradiated, colored amorphous WO_3 thin films. They argued that the band should originate from W5d states, i.e., conduction band states that are empty in intrinsic WO_3 . The population of such states was parallel to the appearance of a W(V) signal in the W4f core levels spectra. De Angelis and Schiavello [113] reported a similar signal in the valence band of several substoichiometric tungsten oxides, again evidencing the filling of the W5d states. In 1978, Colton et al. [114] explicitly connected oxygen removal from WO_3 thin films to the appearance of a small band in the valence spectra. Any additional electron resulting from oxygen removal would occupy the normally empty (in a purely ionic description of the WO_3 crystal) W5d states, which would mean the reduction of W(VI) to W(V). The following year, Salje et al. [115] had to use several components to fit the XPS spectra of WO_3 single crystals reduced by ion bombardment. In 1981, Bringans et al. [116] investigated the (001) surfaces of monoclinic WO_3 by ultraviolet photoemission spectroscopy (UPS). They observed that, upon bombardment of the surfaces with electrons, argon ions and oxygen ions, a density of states appeared in the spectra in the energy gap. By referring to previous studies, where the preferential removal of oxygen had been observed for several oxide surfaces, the authors concluded that the newly appearing density of states was due to generated oxygen vacancies. In a following paper, Höchst and Bringans [117] again attributed to oxygen vacancies the appearance of a density of states in the energy gap of WO_3 thin films grown by evaporation. When the films were annealed at increasing temperatures, the peak increased and the films finally became metallic. Exposure to atomic oxygen resulted in the disappearance of the peak and, following an interpretation of the peak, it was determined that this was due to the presence of oxygen vacancies. Since then, oxygen vacancies and their spectroscopic signature through several W states have progressively become accepted. In a particularly clear and important example, Dixon et al. [118] carried out a series of investigations on WO_3 surfaces using several techniques. In one of these papers, this group employed resonant photoemission to investigate the (001) surface of cleaved crystals of monoclinic WO_3 , with the photon energy tuned to resonance with the W5d states.

After mild ion bombardment, a W5d structure clearly emerged, attributed to oxygen removal from the surface and the consequent filling of the otherwise empty W5d band, in agreement with the early studies reported above. The analysis of the W5d region (valence band spectra) after prolonged bombardment showed complex spectra featuring several components, attributed to $5d^0$, $5d^1$ and $5d^2$ states, the last two being associated with the effects of ion bombardment. Prolonged ion bombardment resulted in the enhancement of the described spectral features. In particular, the W5d band resulted in a much higher

density of states at the Fermi level, with the pronounced metallic nature of the surface. Analogously, the XPS W4f core level presented a complex structure after ion bombardment, requiring three doublets for a correct fit. Such doublets were associated with the appearance of the $5d^0$, $5d^1$ and $5d^2$ components in the valence band spectra, and therefore were associated with the reduction of the surface undergoing the bombardment. The authors could therefore associate different surface structures to the bombardment intensity. This achievement represented progress in terms of the knowledge of the surface chemistry of WO_3 with respect to early works, where complex XPS spectra had already been interpreted in terms of oxygen vacancies. The importance of the $W5p_{3/2}$ component in the fitting of the W4f region was also evidenced. An example of such fittings is reported in Figure 4, where the whole set of oxidations states, from W(IV) to W(VI), and the $W5p_{3/2}$ component, were used. As a final example, the photoemission study on WO_3 polycrystalline thin films by Bussolotti et al. can be quoted [119]. Even in this case, the presence of oxygen vacancies, whose concentration could be modulated by annealing in ultra-high vacuum, was associated with the complex line shape of the W4f photoemission signal.

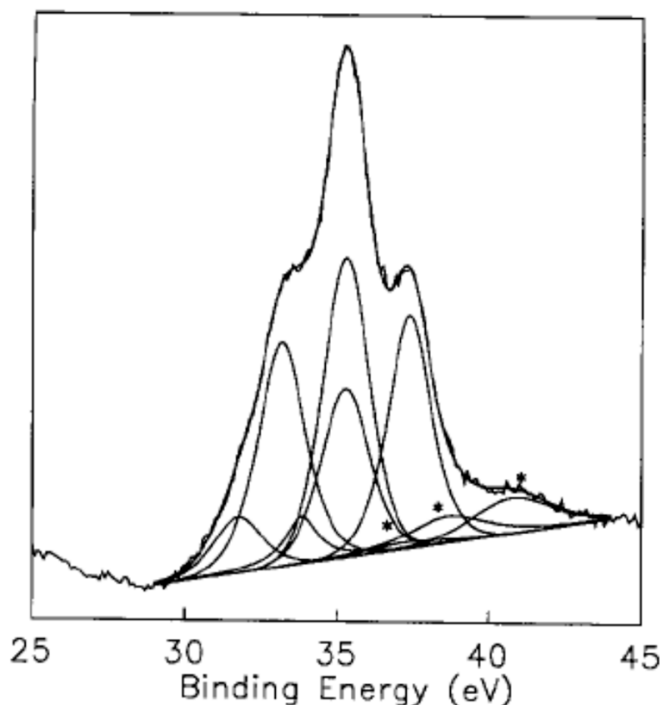


Figure 4. Fitting of the W4f energy region. The stars indicated the $5p_{3/2}$ which had to be added to the $4f_{7/2} + 4f_{5/2}$ doublets for a correct fit of the experimental curve. Reprinted from Figure 6a in Surf. Sci., Vol. 399: R.A. Dixon, J.J. Williams, D. Morris, J. Rebane, F.H. Jones, R.G. Egdell, S.W. Downes, “Electronic states at oxygen deficient $WO_3(001)$ surfaces: a study by resonant photoemission”, pp. 199–211, Copyright (1998), with permission from Elsevier. License number: 5235331217794.

Another interesting technique which involves directly visualizing the structure of reduced WO_3 surfaces is scanning tunneling microscopy. Jones et al. [120] studied the structure of the (001) surface of cleaved monoclinic WO_3 crystals before and after ion bombardment and annealing in UHV conditions. They argued that, in the stoichiometric (001) surface, half of the oxygens are missing in order to avoid the situation of a surface with divergent energy (Tasker’s rule). This requirement results in the experimental observation of surface $\sqrt{2} \times \sqrt{2}$ R45° reconstruction. Such surfaces easily lose oxygen ions, and the defects organize in linear structures, with the W ions adjacent to which assuming the W(V) state. Figure 5 shows models of the possible reconstructions of the (001) monoclinic surface.

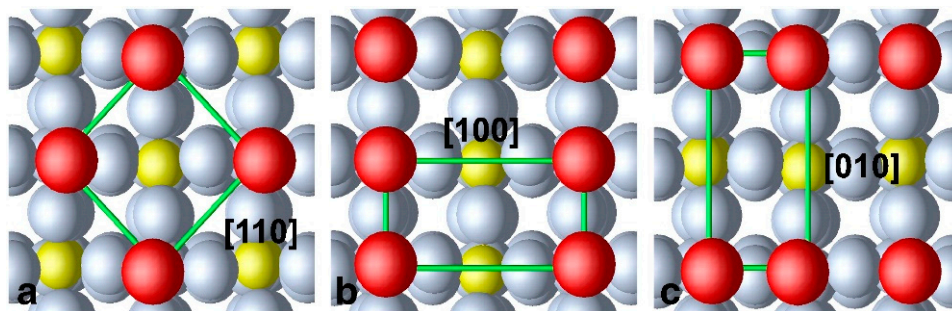


Figure 5. Top view of O-terminated surface for the reconstructions: (a) $(\sqrt{2} \times \sqrt{2} R45^\circ)$, (b) (2×1) and (c) (1×2) . Red spheres are surface oxygen atoms, while yellow and gray spheres are tungsten and other oxygen atoms, respectively. Reprinted from Surf. Sci., Vol. 606: C. Lambert-Mauriat, V. Oison, L. Saadi, K. Aguir, “Ab initio study of oxygen point defects on tungsten trioxide surface”, pp. 40–45, Copyright (2012) with Permission from Elsevier. License number: 5227571391232.

3.2.2. First Principles Modeling of Oxygen Vacancies in WO_3

The ubiquitous appearance of oxygen vacancies, and their impact on the physical properties of WO_3 , have prompted widespread interest in the understanding of the origin and electronic properties of such defects. While the γ and δ phases are the main interest in terms of gas sensing, several thorough theoretical investigations of various polymorphs exist. Once again, the simple cubic structure was considered in early studies [121,122]. Later on, Chatten et al. [123] employed the Perdew–Becke–Ernzerhof functional in the DFT framework for studying several WO_3 polymorphs, both intrinsic and oxygen-deficient. The structural relaxation after introducing an oxygen vacancy resulted in increased WW distance across the vacancy and in a modification of the WO bond length splitting along all the directions. Such modification resulted in new bonding–antibonding interactions with different effects depending on the considered direction. They also established that for all the studied polymorphs, the lowest bands of the W5d levels (which in WO_3 roughly gives rise to the conduction band, while the valence band is mainly contributed to by the O2p levels) crossed the Fermi level, so the systems had a metallic nature. This is one of the still most intensely debated topics in investigations of the electronic structure of WO_3 and is of outmost importance since it is closely related to the understanding of electrochromism in WO_3 [124]. Later on [125], Lambert-Mauriat and Oison [125] used both LDA and GGA functionals to study the oxygen vacancies of γ - WO_3 . They confirmed the metallic nature of the oxygen-deficient phase due to the filling of the bottom of the conduction band and, hence, to the partial filling of the W5d states contributing to it. Interestingly, they considered different vacancies depending on the specific oxygen removed from the considered cell. Indeed, in the monoclinic structure there are three non-equivalent oxygens, depending on the crystallographic direction. In 2011, Wang et al. [126] argued that the metallic nature of oxygen-deficient WO_3 could be due to the use of standard functionals in DFT, resulting in the underestimation of the band gap and therefore resulting in the aforementioned position of the Fermi level in the conduction band. For this reason, they used hybrid functionals in the DFT frame, together with the distinction of the oxygen vacancies depending on the crystallographic direction. They established that a semiconductor-to-metal transition occurs with an increase in the concentration of the oxygen vacancies. For $WO_{2.94}$ (diluted case), the defects gave rise to a band clearly localized into the band gap, with a large separation from the bottom of the conduction band in the case of vacancies formed along all the axes. For $WO_{2.88}$, the levels of the vacancies formed along the x and y axes crossed the Fermi level. For the vacancies along the z axis, the system remained semiconductive. Since the formation energy of the vacancies was independent from the direction in the lattice, it could be argued that a population formed by the three kinds of vacancies could have been expected. This approach was refined later on [127] by using a larger supercell and a different functional. In this more diluted vacancy configuration, the authors found

that the vacancy formed along the x axis is strongly localized in the vacancy void. The vacancies along the other axes feature a triplet ground state with a shallower nature with respect to the vacancy on the x axis. The excess charge was distributed among the W5d states along the WOW chain. Above all, the vacancy on the z axis had a clear conductive nature, which was interpreted as the basis of the always-invoked relationship between WO_3 electrical conductivity and oxygen vacancies. Mehmood et al. [128] and Migas et al. [129] confirmed merging of the vacancy levels with the conduction band in the case of cubic and γ -monoclinic WO_3 . It can be seen how complex investigations into the physical properties of WO_3 can be and how they critically depending on the chosen model.

Until now, bulk oxygen vacancies have been considered. Such investigations are instructive since they concerns the complex interplay between structural and electronic properties in WO_3 . However, it is more immediate in the context of the field of chemosensors field to consider surface vacancies. In this case, an increasing number of studies have been appearing in the literature. This interest is prompted by the use of WO_3 in water splitting and other energy related applications. Lambert-Mauriat et al. [130] investigated the oxygen vacancy formation on the (001) surface of γ - WO_3 using DFT. Such a surface was calculated to be the most energetically favorable, and this was later confirmed theoretically [131] and was in agreement with previous experimental evidence [120]. They found that the vacancies have an n-doping effect. This result was attributed to the band gap underestimation by the employed DFT functionals. Another important conclusion was that the adsorption of oxygen was more energetically demanding than the formation of the vacancy, which explains the stability of oxygen-deficient WO_3 in various oxygen atmospheres. The same surface was considered by Albanese et al. [132], who also took into account the non-equivalence of the oxygen species (depending on the crystallographic axes) to be removed for forming a vacancy. They found that the three kinds of vacancies result in defect levels merging with the conduction band (see Figure 6). This is a very important conclusion, corroborating the early experimental attribution of the electrical properties of WO_3 to surface oxygen vacancies. Moreover, the formation of the oxygen vacancy at the c axis was more favorable than the bulk value (with the formation energy lowered by 1.5 eV), justifying the expected non-stoichiometry of annealed surfaces.

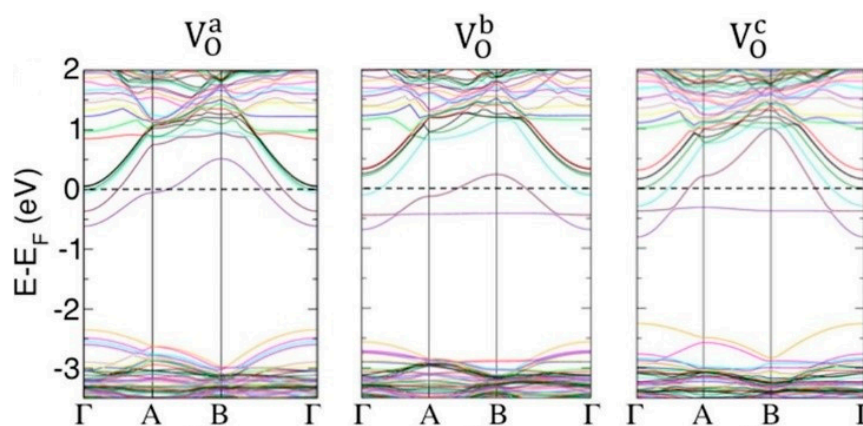


Figure 6. Electronic structure of defective WO_3 surfaces with oxygen vacancies formed along the indicated axes. The Fermi level is represented by a horizontal dashed line at $E-E_F = 0$. Reprinted with permission from Figure 3a in ref. [132]: E. Albanese, C. Di Valentin, Gianfranco Pacchioni, “ H_2O Adsorption on WO_3 and WO_{3-x} (001) Surfaces”, *ACS Appl. Mater. Interfaces* 2017, 9, (27), 23212–23221. Copyright (2017) American Chemical Society.

Summarizing:

1. Oxygen vacancies (both in bulk and on the surface) in WO_3 are ubiquitous and favorably formed during the heat-treatment. Re-healing is not a favorable process, with WO_3 tending to remain oxygen-defective;

2. There is theoretical evidence that oxygen vacancies are anisotropic, with the formation energy depending on the particular crystallographic axis. However, a distribution of all the kinds of vacancies can be expected. The vacancies confer electrical conductivity to WO_3 . The most energetically favorable surface of monoclinic WO_3 is the (001).

3.2.3. Surface Oxygen Vacancies in WO_3 and Adsorption Properties Experimental Studies

The catalytic properties of reduced tungsten oxides were established several years ago [133]. An important feature of WO_3 surfaces is the presence of strong Lewis sites, which play an essential role in the adsorption of a gaseous species in catalysis and, therefore, are of paramount importance for sensors as well [134].

Ramis et al. [135] prepared a “pseudocubic phase” of WO_3 by processing ammonium paratungstate. The investigated samples were initially a mixture of the hexagonal and a “pseudocubic phase”. The latter was converted after heat-treatment at 748 K to what was described as a “poorly crystallized pseudocubic phase”. The phase determination was uncertain between the monoclinic and orthorhombic WO_3 . The investigation of the surface sites was carried out by the adsorption of molecular probes followed by FTIR analysis after evacuation of the samples in the FTIR cell at a maximum temperature of 373 K. Evidence was provided for very strong Lewis sites, which were identified by the authors as surface W^{6+} ions, coordinatively unsaturated. Later on, Kanan et al. [136], using similar techniques, investigated the surface of monoclinic WO_3 . They confirmed the Lewis acidity of the surface and, with respect to ref. [135], they could evacuate the sample at 400 °C. However, a decrease of the Lewis sites by 50% was already observed after evacuation at 150 °C, which was attributed to surface reduction. Instead, adsorbed water did not seem to play any role in the modification of the Lewis sites. The role of the acidic W surface sites was confirmed by the following desorption studies.

Using calibrated thermal desorption spectroscopy, Ma et al. [137] studied the desorption of methanol from both oxidized and reduced $\gamma\text{-WO}_3$ (001) thin film surfaces. They found that, on surfaces oxidized by heat-treatment at a high temperature, methanol was adsorbed onto strongly acidic sites, probably coordinatively unsaturated W(V) sites. No dissociation of the molecule occurred. In contrast, methanol dissociation occurred over the reduced surfaces. The authors attributed this behavior to the increased basicity of the bridging oxygens onto the reduced surface. Such oxygen species would be involved in the dissociation step together with the W(V) sites that are the adsorption site for methanol. In a later paper, Ma and Frederick [138] investigated the desorption of ethanol and 2-propanol from the same surfaces. They found that desorption from the reduced surfaces occurred at higher temperatures than for oxidized surfaces at any coverage value. At lower temperatures, the desorption products were alcohol molecules, while a second desorption channel generated alkenes and water. Water desorption was also investigated and, again, the desorption temperature was higher for reduced surfaces than for the oxidized ones. Water dissociation was not observed.

First Principles Modeling of Adsorption onto WO_3 Surfaces

In 2011, Ling et al. [139] used the Perdew–Burke–Ernzerhof (PBE) functional to investigate the adsorption of hydrogen (atomic and molecular) and methanol onto various surfaces, among which defect-free (001) ϵ -monoclinic WO_3 was included. They considered as adsorption sites two oxygen sites (terminal $\text{O}_{1\text{C}}$ and bridging $\text{O}_{2\text{C}}$) and the coordinatively unsaturated $\text{W}_{5\text{c}}$ site. The authors reported more favorable atomic hydrogen adsorption onto the oxygen sites, with comparable adsorption energies. In the case of molecular hydrogen, dissociation onto $\text{O}_{1\text{C}}$ or onto $\text{O}_{1\text{C}} + \text{O}_{2\text{C}}$ was found to be the only energetically favorable process. The most favorable outcome was hydrogen dissociation onto the $\text{O}_{1\text{C}} + \text{O}_{1\text{C}}$ sites. The authors also considered desorption of a water molecule from the surface (water results from the recombination of the hydroxyl groups formed from hydrogen dissociation) which resulted in surface reduction. In the case of methanol, no dissociation

was predicted, and this was in agreement with the aforementioned experimental studies. Unfavorable methanol dissociation onto the γ -monoclinic (001) surface was confirmed later on [140] by the same group. In 2012, Wang et al. [141] re-examined the problem of hydrogen adsorption by considering the γ -monoclinic (001) surface and implementing the DFT scenario with the hybrid B3LYP functional. The reason for this was the need to avoid bandgap underestimation using the standard DFT methods. In the case of atomic hydrogen, the authors considered several surface oxygen configurations. For 1-coordinated, top O_{1t} oxygen, they found that the proton releases an electron to the nearby W atom, giving rise to a state 0.44 eV below the bottom of the conduction band. In the case of the newly formed H-O bonds onto the in-plane oxygen atoms, this resulted in more delocalized states which were, to different extents, merged with the conduction band. The adsorption energies were similar for all the considered configurations, suggesting the favored migration of the proton over the surface. In the case of molecular hydrogen, the various considered configurations gave rise to endothermic dissociation processes, in contrast with ref. [139]. The authors attributed the discrepancy to several factors, including the different functional employed in DFT implementation and the different WO_3 crystallographic phase. Later on [132], the same group investigated the adsorption of water onto the stoichiometric and oxygen deficient (001) surface of γ -monoclinic WO_3 . They found that, on the perfect surface, the adsorption of molecular water is favored over dissociation, and that the latter is favorable only for high surface coverage. In such a case, the surface is completely covered by a network of hydrogen bonded W-OH groups. In the case of the oxygen defective surface, the authors distinguished among various vacancy topologies, as discussed at the end of Section 3.2.2. They did not find relevant differences with respect to the stoichiometric surface, with adsorption still favored with respect to dissociation. Interestingly, the authors reexamined the problem of hydrogen dissociation onto defective WO_3 . In fact, the final water configuration after adsorption is equivalent to adsorbing hydrogen onto the W_{5c} site of a stoichiometric surface (the water oxygen refilling the oxygen vacancy). With respect to their previous work [141], they found exothermic hydrogen dissociation onto terminal, 1-coordinated O_{1c} ions. Heterolytic dissociation was less favorable. The discrepancy was explained on the basis of the small cell previously used. The most important conclusion was that, if water desorption could be modeled as hydrogen dissociation, and the latter, as evidenced by the authors, introduces states merged with the conduction band, the overall effect of water desorption is surface reduction. On the other hand, Zhang et al. [142] confirmed that water adsorption is more favorable than dissociation onto the stoichiometric, monoclinic WO_3 (001) surface, with the energy difference between the two processes decreasing with increased water coverage. However, diverging from previous studies, they found that dissociation is an exothermic process onto defective surfaces. Finally, Hurtado-Aular et al. [143] recently confirmed that water adsorption is more favorable than dissociation over stoichiometric (001) and (100) γ -monoclinic surfaces. Dissociation was more and more favored with increasing surface coverage by water molecules. The perusal of these studies shows the difficulties involved in modeling the surface chemistry of oxides such as WO_3 .

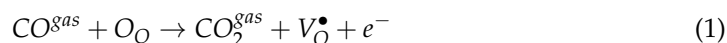
Summarizing:

1. Experimentally, the surface of monoclinic WO_3 contains strongly acidic W sites; the reduction of the surface strongly favors adsorption of methanol and water. Methanol dissociation takes place on reduced surfaces, which is not the case with water.
2. Theoretically speaking, water adsorption is generally calculated to be more favorable than dissociation. However, water desorption resulting from hydrogen dissociation results in surface reduction. We can take this result as an indication that, reciprocally, water dissociation on reduced WO_3 surfaces may result in the healing of oxygen vacancies. While apparently unfavorable in the DFT scenario, water dissociation cannot be neglected from experimental studies where an electrical bias is also applied, such as in the case of chemoresistive sensors.

4. Mechanistic Studies of WO₃ Sensor Properties

The study of sensing pathways with WO₃ based devices is much less developed than for SnO₂, despite an increasing number of works dealing with WO₃ sensors, as briefly seen in Section 2. Therefore, the aim of this section is to review the available results and, finally, to try to connect state of the art studies with the previous sections, highlighting possible further developments in terms of pursuable research lines and potentially applicable methodologies.

The first mechanistic study was published in 2010 by Hubner et al. [144]. The authors performed CO sensing measurements both in presence and absence of oxygen, and simultaneously recorded CO₂ production in the cell exhaust. Importantly, the authors also performed measurements in the absence of CO for the purpose of excluding any catalytic effect from the Pt electrodes. This issue is as important as oversight in sensor studies and should be more systematically assessed. The response to CO in the absence of oxygen (O₂ concentration < 3 ppm) ranged over one order of magnitude for CO concentrations from 10 to 100 ppm. The authors concluded that surface reduction by CO occurred, according to the following equation:



where CO^{gas} is the target gas, O_O is a regular oxygen lattice site, CO₂^{gas} is the gaseous by-product, V_O[•] is a singly ionized oxygen vacancy and e[−] is the electron released to the conduction band, finally increasing the conductance. Slow recovery was observed, attributed to surface re-oxidation with the residual oxygen in the cell. This behavior was markedly different from that of SnO₂, where direct reduction of the surface by CO was not observed. From this early study, we can already conclude that the concentration of oxygen vacancies is of paramount importance in determining the WO₃ sensor response. With an increase in the vacancy concentration, the surface will oppose more and more to further reduction, therefore hampering the sensor response. From the previous discussion, we know that the surface of as-prepared WO₃ typically contains oxygen vacancies and that this is an energetically favorable surface configuration. Therefore, planning to use a perfectly stoichiometric WO₃ surface would result in a high response due to the availability of the maximum possible concentration of removable oxygens. However, full recovery would not be a favorable process, thus hampering the repeatability of the performance. In 2016 [145], the same group investigated another important difference with respect to SnO₂ sensing. While exposure to water vapor has been known for long time to decrease the electrical resistance of SnO₂ [146], the authors had already observed an opposite effect for WO₃ [147]. First of all, an in situ XRD study was conducted to verify the crystal phase stability of the tested γ -monoclinic WO₃ devices at the operating temperatures. A reversible monoclinic \rightarrow orthorhombic was observed at about 300 °C during the heating stage, which was the operating temperature of the sensors. Upon cooling, the reverse transition occurred at about 272 °C. This essential study, an example of which is reported in Figure 7, is probably one of the very few examples for WO₃. The importance of a correct phase determination for understanding the sensing properties of WO₃ has already been outlined in Section 3.1. The second result of the study was the confirmation of a decrease in electrical resistance with increasing levels of humidity at 300 °C. It was shown that, in agreement with their previous study, humidity did not interfere with the CO operation (the sensor signal increased) while a decrease in the NO₂ response was observed with increasing humidity. Finally, by operando DRIFT (Diffuse Reflectance Infrared Fourier Transform) spectroscopy the authors investigated the surface reactions of CO and NO₂ with the devices during the sensing operation. The conclusion was that CO resulted in surface reduction by extracting oxygen from WO₃, while NO₂ healed the surface oxygen vacancies, thus decreasing the signal. Very importantly, the authors concluded that the effect of humidity was due to vacancy healing by the oxygen contained in the water molecule, in perfect agreement with the conclusions of the first principles studies discussed in the previous section (there, water desorption resulted in surface reduction). However, the experimentally determined WO₃ phase (orthorhombic) in ref. [145] was different from that in ref. [132]. This additional issue

was considered in a following work [148] by the same group, where experimental DRIFT studies were coupled with first principles DFT modeling onto the orthorhombic WO_3 surface. In this complex experimental case, where the concurring adsorption of oxygen species was also demonstrated, the authors also confirmed that the increase in the resistance of the sensors at 300 °C was due to water adsorption on the surface, resulting in the healing of oxygen vacancies and hydrogen generation. Hydrogen production was also measured experimentally. Finally [149], such sensing properties of WO_3 were demonstrated to be independent of the synthesis process and, overall, closely connected with the presence of oxygen vacancies. This last conclusion gave rise to a negative outlook regarding the achievability of selective sensors.

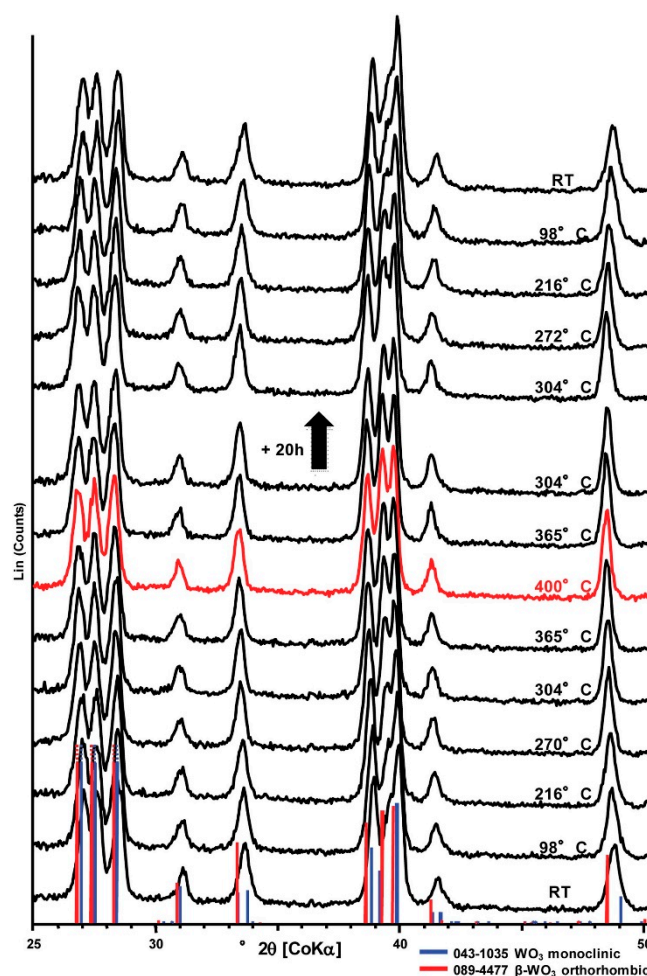


Figure 7. XRD patterns recorded on a WO_3 sample during in situ heating up to 400 °C, followed by holding for 20 h at 304 °C and cooling to room temperature. The phase transition from monoclinic to orthorhombic at about 300 °C is clearly visible. Reprinted from *Sens. Actuators, B: Chem.*, Vol. 237, A. Staerz, C. Berthold, T. Russ, S. Wicker, U. Weimar, N. Barsan, “The oxidizing effect of humidity on WO_3 based sensors”, pp. 54–58, Copyright (2016) with permission from Elsevier. License number: 5247560728197.

The experimental findings on the CO reaction mechanism were confirmed early on by DFT modeling [150], where the authors confirmed direct surface reduction by CO and the formation of oxygen vacancies. Instead, in the same study, ozone sensing was predicted on the basis of oxygen vacancy healing upon the dissociation of the ozone molecules. In the case of NO_2 , Saadi et al. [151] showed that, in agreement with the previously mentioned experimental findings, the likely pathway consists in oxygen vacancy healing by NO_2 , implying an increase in electrical resistance.

5. Conclusions

The present review work has attempted to critically analyze several aspects of the physics and chemistry of WO_3 related to the sensing properties of this material. Considerable obstacles remain to be overcome, however. Therefore, in the conclusions, the established facts will first be mentioned, and possible further directions will then be briefly indicated.

The following noteworthy established points emerged:

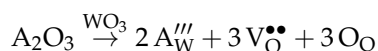
1. The complex crystallographic phase diagram of WO_3 must be taken into account when determining the phase involved in the sensing activity. At room temperature, the as-prepared samples may be constituted by a mixture of γ -monoclinic and δ -triclinic phases, whose speciation can be facilitated by combining XRD and Raman spectroscopy. The investigation of the sensing behavior cannot disregard that at typical operating temperatures, such as 300 °C, the active phase may be the orthogonal one. Therefore, determining the phase composition of the as-prepared samples can be insufficient for studying sensing properties.
2. The oxygen vacancies dominate the physical properties of WO_3 . From first principles modeling, it appears that both bulk and surface vacancies share some features: the formation energy and the electronic effect of the vacancies depend on the crystallographic direction along which they are formed. However, an increasingly accepted view is that at least some of the vacancy levels merge with the Fermi level, explaining the electrical conductivity of oxygen-deficient WO_3 , in agreement with experimental findings. From an experimental point of view, XPS analysis is extremely useful in distinguishing the various W oxidation states connected to the presence of oxygen vacancies. However, such a technique must be used carefully. For instance, the fitting of the W4f region cannot exclude a W5p_{3/2} component. Analysis of the valence band spectra may provide useful information about the presence of oxygen vacancies.
3. Experimental studies into the sensing mechanisms of WO_3 have radically modified the common view of chemoresistive sensing. In the case of CO sensing, the direct generation of oxygen vacancies onto the WO_3 surface has been solidly supported. In the case of NO_2 , the healing of surface vacancies with NO by-product has been backed up by considerable evidence. These conclusions deeply question the usual hypothesis regarding the charge depletion layer by oxygen adsorption and its subsequent modulation by the gas analyte. This is a general indication to carefully check for the applicability of widespread models.
4. This final conclusion is of paramount importance: if oxygen vacancies display such a dominant role and they are present in every oxide, even though to different extents and with different concentrations and structures, the achievability of selectivity by chemoresistive oxide sensors is deeply questionable.

On the other hand, the behavior of WO_3 still appears to be far from elucidated, with the following possible issues to be solved and research directions to be pursued.

5. If direct extraction of oxygen from the WO_3 surface by CO (Section 4) was a surprising result, even direct vacancy healing by NO_2 remarkably differs from the widespread mechanism based on NO_2 adsorption/desorption. It seems that such a mechanism still has to be reinforced by suitable measurements of the sensor exhaust during the NO_2 tests.
6. In turn, such mechanistic conclusions indicate the need for a deep revision of the currently accepted models. This can only be done by intensifying the operando investigation of the sensor operation and the effective identification of the evolved species.
7. DFT modeling has been demonstrated as a powerful tool for verifying hypotheses about the surfaces and structures of WO_3 . The most commonly considered surface is the (001) plane in the γ -monoclinic phase, which is the most favorable and the most immediately formed upon cleaving single crystals. However, in a polycrystalline nanopowder, several other exposed facets are commonly present. In this sense, there

are not many studies of the energy ordering [131] of the exposed crystal planes and of the oxygen vacancy formation energy. This topic needs to be investigated in detail to complete our knowledge of the surface properties of WO₃. Other crystallographic phases, such as the orthorhombic phase, should also be considered.

8. Moreover, still there are very few DFT studies directly related to WO₃ sensing. It would be helpful to obtain a catalogue of the most favorable adsorption sites for several gaseous analytes of interest. This is more and more desirable given the remarkably improved computing capabilities currently available.
9. If oxygen vacancies are vitally important in establishing the sensing behavior of WO₃, then any improvement of WO₃ sensors must be based on understanding and controlling such vacancies. “Understanding” means that a suitable catalogue of characterization techniques must emerge as a standard toolbox for establishing the vacancy concentration, topology and electronic structure. Therefore, XPS should ideally be complemented by other techniques, such as electron paramagnetic resonance, cathodoluminescence, etc. [152].
10. “Controlling” the vacancies means that the synthesis should be tailored toward the achievement of a given distribution of oxygen vacancies. Currently, treatments in reduced atmospheres are employed for preparing oxygen-deficient WO₃. However, such structures are naturally amenable to being reoxidized during the sensor operation. Another strategy could be the designed introduction of dopants into the structure of WO₃. For instance, let A₂O₃ be the oxide of a trivalent cation. The incorporation equation for substitutional defects for such an oxide into WO₃ is, in Kröger–Vink notation:



It can be seen that the concentration of the A cation may precisely pin the oxygen vacancies concentration. Therefore, the synthesis effort can be directed towards the achievement of a stable solid solution, given the suitable metal cations that can be incorporated into the WO₃ structure. This is just a simple suggestion, mainly aimed to further show that cooperation between sensor science and other fields (in this case, structural chemistry) is more and more essential for understanding and enhancing the operation of WO₃-based devices.

Funding: This research received no external funding.

Institutional Review Board Statement: Not applicable.

Informed Consent Statement: Not applicable.

Data Availability Statement: Not applicable.

Conflicts of Interest: The author declares no conflict of interest.

References

1. Zeb, S.; Sun, G.X.; Nie, Y.; Xu, H.Y.; Cui, Y.; Jiang, X.C. Advanced developments in nonstoichiometric tungsten oxides for electrochromic applications. *Mater. Adv.* **2021**, *2*, 6839–6884. [[CrossRef](#)]
2. Granqvist, C.G. Electrochromic Oxides: A Unified View. *Solid State Ionics* **1994**, *70*, 678–685. [[CrossRef](#)]
3. Wang, S.F.; Fan, W.R.; Liu, Z.C.; Yu, A.B.; Jiang, X.C. Advances on tungsten oxide based photochromic materials: Strategies to improve their photochromic properties. *J. Mater. Chem. C* **2018**, *6*, 191–212. [[CrossRef](#)]
4. Janaky, C.; Rajeshwar, K.; de Tacconi, N.R.; Chanmanee, W.; Huda, M.N. Tungsten-based oxide semiconductors for solar hydrogen generation. *Catal. Today* **2013**, *199*, 53–64. [[CrossRef](#)]
5. Shabdan, Y.; Markhabayeva, A.; Bakranov, N.; Nuraje, N. Photoactive Tungsten-Oxide Nanomaterials for Water-Splitting. *Nanomaterials* **2020**, *10*, 1871. [[CrossRef](#)] [[PubMed](#)]
6. Bignozzi, C.A.; Caramori, S.; Cristino, V.; Argazzi, R.; Meda, L.; Tacca, A. Nanostructured photoelectrodes based on WO₃: Applications to photooxidation of aqueous electrolytes. *Chem. Soc. Rev.* **2013**, *42*, 2228–2246. [[CrossRef](#)] [[PubMed](#)]
7. Wang, Y.D.; Tian, W.; Chen, C.; Xu, W.W.; Li, L. Tungsten Trioxide Nanostructures for Photoelectrochemical Water Splitting: Material Engineering and Charge Carrier Dynamic Manipulation. *Adv. Funct. Mater.* **2019**, *29*, 1809036. [[CrossRef](#)]

8. Dong, P.Y.; Hou, G.H.; Xi, X.U.; Shao, R.; Dong, F. WO₃-based photocatalysts: Morphology control, activity enhancement and multifunctional applications. *Environ. Sci. Nano* **2017**, *4*, 539–557. [[CrossRef](#)]
9. Yang, G.; Zhu, X.T.; Cheng, G.; Chen, R.; Xiong, J.Y.; Li, W.J.; Wei, Y.C. Engineered tungsten oxide-based photocatalysts for CO₂ reduction: Categories and roles. *J. Mater. Chem. A* **2021**, *9*, 22781–22809. [[CrossRef](#)]
10. Yadav, A.A.; Hunge, Y.M.; Kang, S.-W. Porous nanoplate-like tungsten trioxide/reduced graphene oxide catalyst for sonocatalytic degradation and photocatalytic hydrogen production. *Surf. Interfaces* **2021**, *24*, 101075. [[CrossRef](#)]
11. Peleyeju, M.G.; Viljoen, E.L. WO₃-based catalysts for photocatalytic and photoelectrocatalytic removal of organic pollutants from water—A review. *J. Water Process. Eng.* **2021**, *40*, 101930. [[CrossRef](#)]
12. Liao, M.J.; Su, L.; Deng, Y.C.; Xiong, S.; Tang, R.D.; Wu, Z.B.; Ding, C.X.; Yang, L.H.; Gong, D.X. Strategies to improve WO₃-based photocatalysts for wastewater treatment: A review. *J. Mater. Sci.* **2021**, *56*, 14416–14447. [[CrossRef](#)]
13. Dutta, V.; Sharma, S.; Raizada, P.; Thakur, V.K.; Khan, A.A.P.; Saini, V.; Asiri, A.M.; Singh, P. An overview on WO₃ based photocatalyst for environmental remediation. *J. Environ. Chem. Eng.* **2021**, *9*, 105018. [[CrossRef](#)]
14. Shinde, P.A.; Jun, S.C. Review on Recent Progress in the Development of Tungsten Oxide Based Electrodes for Electrochemical Energy Storage. *ChemSusChem* **2020**, *13*, 11–38. [[CrossRef](#)] [[PubMed](#)]
15. Zu, D.; Wang, H.Y.; Lin, S.; Ou, G.; Wei, H.H.; Sun, S.Q.; Wu, H. Oxygen-deficient metal oxides: Synthesis routes and applications in energy and environment. *Nano Res.* **2019**, *12*, 2150–2163. [[CrossRef](#)]
16. Shaver, P.J. Activated Tungsten Oxide Gas Detectors. *Appl. Phys. Lett.* **1967**, *11*, 255–257. [[CrossRef](#)]
17. Frühberger, B.; Grunze, M.; Dwyer, D.J. Surface chemistry of H₂S-sensitive tungsten oxide films. *Sens. Actuators B Chem.* **1996**, *31*, 167–174. [[CrossRef](#)]
18. Dwyer, D.J. Surface chemistry of gas sensors: H₂S on WO₃ films. *Sens. Actuators B Chem.* **1991**, *5*, 155–159. [[CrossRef](#)]
19. Sriram, S.R.; Parne, S.; Vaddadi, V.S.C.S.; Edla, D.; Nagaraju, P.; Avala, R.R.; Yelsani, V.; Sontu, U.B. Nanostructured WO₃ based gas sensors: A short review. *Sens. Rev.* **2021**, *41*, 406–424. [[CrossRef](#)]
20. Lei, G.L.; Lou, C.M.; Liu, X.H.; Xie, J.Y.; Li, Z.S.; Zheng, W.; Zhang, J. Thin films of tungsten oxide materials for advanced gas sensors. *Sens. Actuators B Chem.* **2021**, *341*, 129996. [[CrossRef](#)]
21. Bonardo, D.; Septiani, N.L.W.; Amri, F.; Estananto; Humaidi, S.; Suyatman; Yuliarto, B. Review—Recent Development of WO₃ for Toxic Gas Sensors Applications. *J. Electrochem. Soc.* **2021**, *168*, 107502. [[CrossRef](#)]
22. Long, H.W.; Zeng, W.; Zhang, H. Synthesis of WO₃ and its gas sensing: A review. *J. Mater. Sci. Mater. Electron.* **2015**, *26*, 4698–4707. [[CrossRef](#)]
23. Mirzaei, A.; Kim, J.H.; Kim, H.W.; Kim, S.S. Gasochromic WO₃ Nanostructures for the Detection of Hydrogen Gas: An Overview. *Appl. Sci.* **2019**, *9*, 1775. [[CrossRef](#)]
24. Barsan, N.; Weimar, U. Conduction Model of Metal Oxide Gas Sensors. *J. Electroceram.* **2001**, *7*, 143–167. [[CrossRef](#)]
25. Bouchikhi, B.; Chludziński, T.; Saidi, T.; Smulko, J.; Bari, N.E.; Wen, H.; Ionescu, R. Formaldehyde detection with chemical gas sensors based on WO₃ nanowires decorated with metal nanoparticles under dark conditions and UV light irradiation. *Sens. Actuators B Chem.* **2020**, *320*, 128331. [[CrossRef](#)]
26. Wu, R.; Tian, F.H.; Liu, Z.Z.; Xue, X.Y.; Zhang, J.; Zu, J.H. CH₄ activation and sensing on hexagonal WO₃ (001) and (110) surfaces. *Appl. Surf. Sci.* **2019**, *481*, 1154–1159. [[CrossRef](#)]
27. Tian, F.H.; Gong, C.; Wu, R.; Liu, Z.Z. Oxygen density dominated gas sensing mechanism originated from CO adsorption on the hexagonal WO₃ (001) surface. *Mater. Today Chem.* **2018**, *9*, 28–33. [[CrossRef](#)]
28. Gerand, B.; Nowogrocki, G.; Guenot, J.; Figlarz, M. Structural study of a new hexagonal form of tungsten trioxide. *J. Solid State Chem.* **1979**, *29*, 429–434. [[CrossRef](#)]
29. Tian, F.H.; Liu, Z.Z.; Tian, J.; Zhang, Y.F. Oxygen vacancy O-terminated surface: The most exposed surface of hexagonal WO₃ (001) surface. *Chin. Chem. Lett.* **2020**, *31*, 2095–2098. [[CrossRef](#)]
30. Hurtado-Aular, O.; Anez, R.; Sierralta, A.; Calderon, J. Discovering the root of the stability of hexagonal WO₃ surfaces from a periodic DFT perspective. *Appl. Surf. Sci.* **2020**, *506*, 144719. [[CrossRef](#)]
31. Staerz, A.; Weimar, U.; Barsan, N. Understanding the Potential of WO₃ Based Sensors for Breath Analysis. *Sensors* **2016**, *16*, 1815. [[CrossRef](#)] [[PubMed](#)]
32. Akiyama, M.; Tamaki, J.; Miura, N.; Yamazoe, N. Tungsten Oxide-Based Semiconductor Sensor Highly Sensitive to NO and NO₂. *Chem. Lett.* **1991**, *20*, 1611–1614. [[CrossRef](#)]
33. Tamaki, J.; Zhang, Z.; Fujimori, K.; Akiyama, M.; Harada, T.; Miura, N.; Yamazoe, N. Grain-Size Effects in Tungsten Oxide-Based Sensor for Nitrogen-Oxides. *J. Electrochem. Soc.* **1994**, *141*, 2207–2210. [[CrossRef](#)]
34. Kida, T.; Nishiyama, A.; Yuasa, M.; Shimano, K.; Yamazoe, N. Highly sensitive NO₂ sensors using lamellar-structured WO₃ particles prepared by an acidification method. *Sens. Actuators B Chem.* **2009**, *135*, 568–574. [[CrossRef](#)]
35. Kim, S.-J.; Hwang, I.-S.; Choi, J.-K.; Lee, J.-H. Gas sensing characteristics of WO₃ nanoplates prepared by acidification method. *Thin Solid Film.* **2011**, *519*, 2020–2024. [[CrossRef](#)]
36. Wang, Z.; Wang, D.; Sun, J. Controlled synthesis of defect-rich ultrathin two-dimensional WO₃ nanosheets for NO₂ gas detection. *Sens. Actuators B Chem.* **2017**, *245*, 828–834. [[CrossRef](#)]
37. Wang, M.S.; Wang, Y.W.; Li, X.J.; Ge, C.X.; Hussain, S.; Liu, G.W.; Qiao, G.J. WO₃ porous nanosheet arrays with enhanced sensing performance low temperature NO₂ gas. *Sens. Actuators B Chem.* **2020**, *316*, 128050. [[CrossRef](#)]

38. Kim, J.-S.; Yoon, J.-W.; Hong, Y.J.; Kang, Y.C.; Abdel-Hady, F.; Wazzan, A.A.; Lee, J.-H. Highly sensitive and selective detection of ppb-level NO₂ using multi-shelled WO₃ yolk-shell spheres. *Sens. Actuators B Chem.* **2016**, *229*, 561–569. [[CrossRef](#)]
39. You, L.; He, X.; Wang, D.; Sun, P.; Sun, Y.F.; Liang, X.S.; Du, Y.; Lu, G.Y. Ultrasensitive and low operating temperature NO₂ gas sensor using nanosheets assembled hierarchical WO₃ hollow microspheres. *Sens. Actuators B Chem.* **2012**, *173*, 426–432. [[CrossRef](#)]
40. Akamatsu, T.; Itoh, T.; Izu, N.; Shin, W. Preparation of WO₃ nanoplatelet-based microspheres and their NO₂ gas-sensing properties. *J. Ceram. Soc. Jpn.* **2014**, *122*, 674–678. [[CrossRef](#)]
41. An, S.; Park, S.; Ko, H.; Lee, C. Fabrication of WO₃ nanotube sensors and their gas sensing properties. *Ceram. Int.* **2014**, *40*, 1423–1429. [[CrossRef](#)]
42. Qi, J.J.; Gao, S.; Chen, K.; Yang, J.; Zhao, H.W.; Guo, L.; Yang, S.H. Vertically aligned, double-sided, and self-supported 3D WO₃ nanocolumn bundles for low-temperature gas sensing. *J. Mater. Chem. A* **2015**, *3*, 18019–18026. [[CrossRef](#)]
43. Wang, C.; Ding, M.D.; Kou, X.Y.; Guo, L.L.; Feng, C.H.; Li, X.; Zhang, H.; Sun, P.; Sun, Y.F.; Lu, G.Y. Detection of nitrogen dioxide down to ppb levels using flower-like tungsten oxide nanostructures under different annealing temperatures. *J. Colloid Interface Sci.* **2016**, *483*, 314–320. [[CrossRef](#)] [[PubMed](#)]
44. Khan, H.; Zavabeti, A.; Wang, Y.C.; Harrison, C.J.; Carey, B.J.; Mohiuddin, M.; Chrimes, A.F.; De Castro, I.A.; Zhang, B.Y.; Sabri, Y.M.; et al. Quasi physisorptive two dimensional tungsten oxide nanosheets with extraordinary sensitivity and selectivity to NO₂. *Nanoscale* **2017**, *9*, 19162–19175. [[CrossRef](#)] [[PubMed](#)]
45. Harale, N.S.; Dalavi, D.S.; Mali, S.S.; Tarwal, N.L.; Vanalakar, S.A.; Rao, V.K.; Hong, C.K.; Kim, J.H.; Patil, P.S. Single-step hydrothermally grown nanosheet-assembled tungsten oxide thin films for sensitive and selective NO₂ gas detection. *J. Mater. Sci.* **2018**, *53*, 6094–6105. [[CrossRef](#)]
46. Hua, Z.Q.; Tian, C.; Qiu, Z.L.; Li, Y.; Tian, X.M.; Wang, M.J.; Li, E.P. An investigation on NO₂ sensing mechanism and shielding behavior of WO₃ nanosheets. *Sens. Actuators B Chem.* **2018**, *259*, 250–257. [[CrossRef](#)]
47. Beknalkar, S.A.; Patil, V.L.; Harale, N.S.; Suryawanshi, M.P.; Patil, A.P.; Patil, V.B.; Kim, J.H.; Patil, P.S. 2-D to 3-D conversion of WO₃ nanostructures using structure directing agent for enhanced NO₂ gas sensing performance. *Sens. Actuators A Phys.* **2020**, *304*, 111882. [[CrossRef](#)]
48. Song, W.Q.; Zhang, R.; Bai, X.; Jia, Q.Q.; Ji, H.M. Exposed crystal facets of WO₃ nanosheets by phase control on NO₂-sensing performance. *J. Mater. Sci. Mater. Electron.* **2020**, *31*, 610–620. [[CrossRef](#)]
49. Morais, P.V.; Suman, P.H.; Silva, R.A.; Orlandi, M.O. High gas sensor performance of WO₃ nanofibers prepared by electrospinning. *J. Alloys Compd.* **2021**, *864*, 158745. [[CrossRef](#)]
50. Zhang, J.N.; Leng, D.Y.; Zhang, L.Z.; Li, G.; Ma, F.; Gao, J.Z.; Lu, H.B.; Zhu, B.P. Porosity and oxygen vacancy engineering of mesoporous WO₃ nanofibers for fast and sensitive low-temperature NO₂ sensing. *J. Alloys Compd.* **2021**, *853*, 157339. [[CrossRef](#)]
51. Masikini, M.; Chowdhury, M.; Nemraoui, O. Review-Metal Oxides: Application in Exhaled Breath Acetone Chemiresistive Sensors. *J. Electrochem. Soc.* **2020**, *167*, 037537. [[CrossRef](#)]
52. Alizadeh, N.; Jamalabadi, H.; Tavoli, F. Breath Acetone Sensors as Non-Invasive Health Monitoring Systems: A Review. *IEEE Sens. J.* **2020**, *20*, 5–31. [[CrossRef](#)]
53. Li, X.L.; Lou, T.J.; Sun, X.M.; Li, Y.D. Highly sensitive WO₃ hollow-sphere gas sensors. *Inorg. Chem.* **2004**, *43*, 5442–5449. [[CrossRef](#)]
54. Khadayate, R.S.; Sali, V.; Patil, P.P. Acetone vapor sensing properties of screen printed WO₃ thick films. *Talanta* **2007**, *72*, 1077–1081. [[CrossRef](#)] [[PubMed](#)]
55. Chen, D.L.; Hou, X.X.; Li, T.; Yin, L.; Fan, B.B.; Wang, H.L.; Li, X.J.; Xu, H.L.; Lu, H.X.; Zhang, R.; et al. Effects of morphologies on acetone-sensing properties of tungsten trioxide nanocrystals. *Sens. Actuators B Chem.* **2011**, *153*, 373–381. [[CrossRef](#)]
56. Shi, J.C.; Hu, G.J.; Sun, Y.; Geng, M.; Wu, J.; Liu, Y.F.; Ge, M.Y.; Tao, J.C.; Cao, M.; Dai, N. WO₃ nanocrystals: Synthesis and application in highly sensitive detection of acetone. *Sens. Actuators B Chem.* **2011**, *156*, 820–824. [[CrossRef](#)]
57. Liu, S.Y.; Zhang, F.; Li, H.; Chen, T.; Wang, Y.D. Acetone detection properties of single crystalline tungsten oxide plates synthesized by hydrothermal method using cetyltrimethyl ammonium bromide supermolecular template. *Sens. Actuators B Chem.* **2012**, *162*, 259–268. [[CrossRef](#)]
58. Zou, X.X.; Li, G.D.; Wang, P.P.; Su, J.; Zhao, J.; Zhou, L.J.; Wang, Y.N.; Chen, J.S. A precursor route to single-crystalline WO₃ nanoplates with an uneven surface and enhanced sensing properties. *Dalton Trans.* **2012**, *41*, 9773–9780. [[CrossRef](#)]
59. Wang, Z.Y.; Sun, P.; Yang, T.L.; Gao, Y.; Li, X.W.; Lu, G.Y.; Du, Y. Flower-like WO₃ architectures synthesized via a microwave-assisted method and their gas sensing properties. *Sens. Actuators B Chem.* **2013**, *186*, 734–740. [[CrossRef](#)]
60. Chi, X.; Liu, C.B.; Liu, L.; Li, Y.; Wang, Z.J.; Bo, X.Q.; Liu, L.L.; Su, C. Tungsten trioxide nanotubes with high sensitive and selective properties to acetone. *Sens. Actuators B Chem.* **2014**, *194*, 33–37. [[CrossRef](#)]
61. Chen, D.L.; Ge, L.F.; Yin, L.; Shi, H.Y.; Yang, D.W.; Yang, J.; Zhang, R.; Shao, G.S. Solvent-regulated solvothermal synthesis and morphology-dependent gas-sensing performance of low-dimensional tungsten oxide nanocrystals. *Sens. Actuators B Chem.* **2014**, *205*, 391–400. [[CrossRef](#)]
62. Zhang, H.L.; Liu, Z.F.; Yang, J.Q.; Guo, W.; Zhu, L.J.; Zheng, W.J. Temperature and acidity effects on WO₃ nanostructures and gas-sensing properties of WO₃ nanoplates. *Mater. Res. Bull.* **2014**, *57*, 260–267. [[CrossRef](#)]
63. Yin, M.L.; Yu, L.M.; Liu, S.Z. Synthesis of thickness-controlled cuboid WO₃ nanosheets and their exposed facets-dependent acetone sensing properties. *J. Alloys Compd.* **2017**, *696*, 490–497. [[CrossRef](#)]

64. Jia, Q.Q.; Ji, H.M.; Bai, X. Selective sensing property of triclinic WO₃ nanosheets towards ultra-low concentration of acetone. *J. Mater. Sci. Mater. Electron.* **2019**, *30*, 7824–7833. [[CrossRef](#)]
65. Xu, H.Y.; Gao, J.; Li, M.H.; Zhao, Y.Y.; Zhang, M.; Zhao, T.; Wang, L.J.; Jiang, W.; Zhu, G.J.; Qian, X.Y.; et al. Mesoporous WO₃ Nanofibers with Crystalline Framework for High-Performance Acetone Sensing. *Front. Chem.* **2019**, *7*, 7. [[CrossRef](#)] [[PubMed](#)]
66. Chang, X.T.; Xu, S.; Liu, S.; Wang, N.N.; Sun, S.B.; Zhu, X.J.; Li, J.F.; Ola, O.; Zhu, Y.Q. Highly sensitive acetone sensor based on WO₃ nanosheets derived from WS₂ nanoparticles with inorganic fullerene-like structures. *Sens. Actuators B Chem.* **2021**, *343*, 130135. [[CrossRef](#)]
67. Wang, Q.; Cheng, X.; Wang, Y.R.; Yang, Y.F.; Su, Q.; Li, J.P.; An, B.X.; Luo, Y.B.; Wu, Z.K.; Xie, E.Q. Sea urchins-like WO₃ as a material for resistive acetone gas sensors. *Sens. Actuators B Chem.* **2022**, *355*, 131262. [[CrossRef](#)]
68. Tomoki, M.; Jun, T.; Norio, M.; Noboru, Y. Gold-Loaded Tungsten Oxide Sensor for Detection of Ammonia in Air. *Chem. Lett.* **1992**, *21*, 639–642. [[CrossRef](#)]
69. Jimenez, I.; Centeno, M.A.; Scotti, R.; Morazzoni, F.; Arbiol, J.; Cornet, A.; Morante, J.R. NH₃ interaction with chromium-doped WO₃ nanocrystalline powders for gas sensing applications. *J. Mater. Chem.* **2004**, *14*, 2412–2420. [[CrossRef](#)]
70. Jimenez, I.; Centeno, M.A.; Scotti, R.; Morazzoni, F.; Cornet, A.; Morante, J.R. NH₃ interaction with catalytically modified nano-WO₃ powders for gas sensing applications. *J. Electrochem. Soc.* **2003**, *150*, H72–H80. [[CrossRef](#)]
71. Epifani, M.; Andreu, T.; Arbiol, J.; Diaz, R.; Siciliano, P.; Morante, J.R. Chloro-Alkoxide Route to Transition Metal Oxides. Synthesis of WO₃ Thin Films and Powders from a Tungsten Chloro-Methoxide. *Chem. Mater.* **2009**, *21*, 5215–5221. [[CrossRef](#)]
72. Nguyen, V.H.; Vu, V.Q.; Nguyen, D.H.; Kim, D. Preparing large-scale WO₃ nanowire-like structure for high sensitivity NH₃ gas sensor through a simple route. *Curr. Appl. Phys.* **2011**, *11*, 657–661.
73. Wang, G.; Ji, Y.; Huang, X.; Yang, X.; Gouma, P.-I.; Dudley, M. Fabrication and Characterization of Polycrystalline WO₃ Nanofibers and Their Application for Ammonia Sensing. *J. Phys. Chem. B* **2006**, *110*, 23777–23782. [[CrossRef](#)] [[PubMed](#)]
74. Epifani, M.; Andreu, T.; Magaña, C.R.; Díaz, R.; Arbiol, J.; Siciliano, P.; Morante, J.R. From doping to phase transformation: Ammonia sensing performances of chloroalkoxide-derived WO₃ powders modified with chromium. *Sens. Actuators B Chem.* **2010**, *148*, 200–206. [[CrossRef](#)]
75. Ji, H.; Zeng, W.; Xu, Y.; Li, Y. Nanosheet-assembled hierarchical WO₃ flower-like nanostructures: Hydrothermal synthesis and NH₃-sensing properties. *Mater. Lett.* **2019**, *250*, 155–158. [[CrossRef](#)]
76. Liu, G.K.; Zhu, L.J.; Yu, Y.M.; Qiu, M.; Gao, H.J.; Chen, D.Y. WO₃ nanoplates for sensitive and selective detections of both acetone and NH₃ gases at different operating temperatures. *J. Alloys Compd.* **2021**, *858*, 157638. [[CrossRef](#)]
77. Cho, Y.H.; Kang, Y.C.; Lee, J.-H. Highly selective and sensitive detection of trimethylamine using WO₃ hollow spheres prepared by ultrasonic spray pyrolysis. *Sens. Actuators B Chem.* **2013**, *176*, 971–977. [[CrossRef](#)]
78. Zhai, C.; Zhu, M.; Jiang, L.; Yang, T.; Zhao, Q.; Luo, Y.; Zhang, M. Fast triethylamine gas sensing response properties of nanosheets assembled WO₃ hollow microspheres. *Appl. Surf. Sci.* **2019**, *463*, 1078–1084. [[CrossRef](#)]
79. Han, Y.T.; Liu, Y.; Su, C.; Chen, X.W.; Zeng, M.; Hu, N.T.; Su, Y.J.; Zhou, Z.H.; Wei, H.; Yang, Z. Sonochemical synthesis of hierarchical WO₃ flower-like spheres for highly efficient triethylamine detection. *Sens. Actuators B Chem.* **2020**, *306*, 127536. [[CrossRef](#)]
80. Hu, Q.; He, J.Q.; Chang, J.Y.; Gao, J.M.; Huang, J.H.; Feng, L. Needle-Shaped WO₃ Nanorods for Triethylamine Gas Sensing. *ACS Appl. Nano Mater.* **2020**, *3*, 9046–9054. [[CrossRef](#)]
81. Hamdi, H.; Salje, E.K.H.; Ghosez, P.; Bousquet, E. First-principles reinvestigation of bulk WO₃. *Phys. Rev. B* **2016**, *94*, 245124. [[CrossRef](#)]
82. Vogt, T.; Woodward, P.M.; Hunter, B.A. The High-Temperature Phases of WO₃. *J. Solid State Chem.* **1999**, *144*, 209–215. [[CrossRef](#)]
83. Woodward, P.M.; Sleight, A.W.; Vogt, T. Structure refinement of triclinic tungsten trioxide. *J. Phys. Chem. Solids* **1995**, *56*, 1305–1315. [[CrossRef](#)]
84. Woodward, P.M.; Sleight, A.W.; Vogt, T. Ferroelectric Tungsten Trioxide. *J. Solid State Chem.* **1997**, *131*, 9–17. [[CrossRef](#)]
85. Salje, E.K.H.; Rehmann, S.; Pobell, F.; Morris, D.; Knight, K.S.; Herrmannsdörfer, T.; Dove, M.T. Crystal structure and paramagnetic behaviour of ε-WO_{3-x}. *J. Phys. Condens. Matter* **1997**, *9*, 6563–6577. [[CrossRef](#)]
86. Salje, E. Structural phase transitions in the system WO₃-NaWO₃. *Ferroelectrics* **1976**, *12*, 215–217. [[CrossRef](#)]
87. Diehl, R.; Brandt, G.; Saije, E. The crystal structure of triclinic WO₃. *Acta Crystallogr. Sect. B Struct. Crystallogr. Cryst. Chem.* **1978**, *34*, 1105–1111. [[CrossRef](#)]
88. Salje, E.; Viswanathan, K. Physical properties and phase transitions in WO₃. *Acta Crystallogr. Sect. A Cryst. Phys. Diffr. Theor. Gen. Crystallogr.* **1975**, *31*, 356–359. [[CrossRef](#)]
89. Tanisaki, S. On the Phase Transition of Tungsten Trioxide below Room Temperature. *J. Phys. Soc. Jpn.* **1960**, *15*, 566–573. [[CrossRef](#)]
90. Loopstra, B.O.; Rietveld, H.M. Further refinement of the structure of WO₃. *Acta Crystallogr. Sect. B Struct. Sci. Cryst. Eng. Mater.* **1969**, *25*, 1420–1421. [[CrossRef](#)]
91. Loopstra, B.O.; Boldrini, P. Neutron diffraction investigation of WO₃. *Acta Crystallogr.* **1966**, *21*, 158–162. [[CrossRef](#)]
92. Cazzanelli, E.; Vinegoni, C.; Mariotto, G.; Kuzmin, A.; Purans, J. Raman study of the phase transitions sequence in pure WO₃ at high temperature and in H_xWO₃ with variable hydrogen content. *Solid State Ion.* **1999**, *123*, 67–74. [[CrossRef](#)]
93. Salje, E. The orthorhombic phase of WO₃. *Acta Crystallogr.* **1977**, *33*, 574–577. [[CrossRef](#)]
94. Kehl, W.L.; Hay, R.G.; Wahl, D. The Structure of Tetragonal Tungsten Trioxide. *J. Appl. Phys.* **1952**, *23*, 212–215. [[CrossRef](#)]

95. Howard, C.J.; Luca, V.; Knight, K.S. High-temperature phase transitions in tungsten trioxide—the last word? *J. Phys. Condens. Matter* **2001**, *14*, 377–387. [[CrossRef](#)]
96. Hassani, H.; Partoens, B.; Bousquet, E.; Ghosez, P. First-principles study of lattice dynamical properties of the room-temperature $P2_1/n$ and ground-state $P2_1/c$ phases of WO_3 . *Phys. Rev. B* **2022**, *105*, 014107. [[CrossRef](#)]
97. Berak, J.M.; Sienko, M.J. Effect of oxygen-deficiency on electrical transport properties of tungsten trioxide crystals. *J. Solid State Chem.* **1970**, *2*, 109–133. [[CrossRef](#)]
98. Stachiotti, M.G.; Corà, F.; Catlow, C.R.A.; Rodriguez, C.O. First-principles investigation of ReO_3 and related oxides. *Phys. Rev. B* **1997**, *55*, 7508–7514. [[CrossRef](#)]
99. Dickens, P.G.; Whittingham, M.S. The tungsten bronzes and related compounds. *Q. Rev. Chem. Soc.* **1968**, *22*, 30–44. [[CrossRef](#)]
100. Bullett, D.W. Bulk and surface electron states in WO_3 and tungsten bronzes. *J. Phys. C Solid State Phys.* **1983**, *16*, 2197–2207. [[CrossRef](#)]
101. Kopp, L.; Harmon, B.N.; Liu, S.H. Band structure of cubic Na_xWO_3 . *Solid State Commun.* **1977**, *22*, 677–679. [[CrossRef](#)]
102. Bersuker, I.B. Pseudo-Jahn–Teller Effect—A Two-State Paradigm in Formation, Deformation, and Transformation of Molecular Systems and Solids. *Chem. Rev.* **2013**, *113*, 1351–1390. [[CrossRef](#)] [[PubMed](#)]
103. De Wijs, G.A.; De Boer, P.K.; De Groot, R.A.; Kresse, G. Anomalous behavior of the semiconducting gap in WO_3 from first-principles calculations. *Phys. Rev. B* **1999**, *59*, 2684–2693. [[CrossRef](#)]
104. Wang, F.G.; Di Valentin, C.; Pacchioni, G. Electronic and Structural Properties of WO_3 : A Systematic Hybrid DFT Study. *J. Phys. Chem. C* **2011**, *115*, 8345–8353. [[CrossRef](#)]
105. Cazzanelli, E.; Vinegoni, C.; Mariotto, G.; Kuzmin, A.; Purans, J. Low-Temperature Polymorphism in Tungsten Trioxide Powders and Its Dependence on Mechanical Treatments. *J. Solid State Chem.* **1999**, *143*, 24–32. [[CrossRef](#)]
106. Souza-Filho, A.G.; Freire, V.N.; Sasaki, J.M.; Mendes Filho, J.; Julião, J.F.; Gomes, U.U. Coexistence of triclinic and monoclinic phases in WO_3 ceramics. *J. Raman Spectrosc.* **2000**, *31*, 451–454. [[CrossRef](#)]
107. Kuzmin, A.; Purans, J.; Cazzanelli, E.; Vinegoni, C.; Mariotto, G. X-ray diffraction, extended x-ray absorption fine structure and Raman spectroscopy studies of WO_3 powders and $(1-x)WO_{3-y}.xReO_2$ mixtures. *J. Appl. Phys.* **1998**, *84*, 5515–5524. [[CrossRef](#)]
108. Jimenez, I.; Arbiol, J.; Dezanneau, G.; Cornet, A.; Morante, J.R. Crystalline structure, defects and gas sensor response to NO_2 and H_2S of tungsten trioxide nanopowders. *Sens. Actuators B Chem.* **2003**, *93*, 475–485. [[CrossRef](#)]
109. Kaneko, H.; Miyake, K.; Teramoto, Y. Preparation and properties of reactively sputtered tungsten oxide films. *J. Appl. Phys.* **1982**, *53*, 3070–3075. [[CrossRef](#)]
110. Gillet, M.; Lemire, C.; Gillet, E.; Aguir, K. The role of surface oxygen vacancies upon WO_3 conductivity. *Surf. Sci.* **2003**, *532*, 519–525. [[CrossRef](#)]
111. Li, W.; Sasaki, A.; Oozu, H.; Aoki, K.; Kakushima, K.; Kataoka, Y.; Nishiyama, A.; Sugii, N.; Wakabayashi, H.; Tsutsui, K.; et al. Electron transport mechanism of tungsten trioxide powder thin film studied by investigating effect of annealing on resistivity. *Microelectron. Reliab.* **2015**, *55*, 407–410. [[CrossRef](#)]
112. Hollinger, G.; Minh Duc, T.; Deneuve, A. Charge Transfer in Amorphous Colored WO_3 Films Observed by X-Ray Photoelectron Spectroscopy. *Phys. Rev. Lett.* **1976**, *37*, 1564–1567. [[CrossRef](#)]
113. De Angelis, B.A.; Schiavello, M. X-ray photoelectron spectroscopy study of nonstoichiometric tungsten oxides. *J. Solid State Chem.* **1977**, *21*, 67–72. [[CrossRef](#)]
114. Colton, R.J.; Guzman, A.M.; Rabalais, J.W. Photochromism and electrochromism in amorphous transition metal oxide films. *Acc. Chem. Res.* **1978**, *11*, 170–176. [[CrossRef](#)]
115. Salje, E.; Carley, A.F.; Roberts, M.W. The effect of reduction and temperature on the electronic core levels of tungsten and molybdenum in WO_3 and $W_xMo_{1-x}O_3$ —A photoelectron spectroscopic study. *J. Solid State Chem.* **1979**, *29*, 237–251. [[CrossRef](#)]
116. Bringans, R.D.; Höchst, H.; Shanks, H.R. Defect states in WO_3 studied with photoelectron spectroscopy. *Phys. Rev. B* **1981**, *24*, 3481–3489. [[CrossRef](#)]
117. Höchst, H.; Bringans, R.D. Electronic structure of evaporated and annealed tungsten oxide films studied with UPS. *Appl. Surf. Sci.* **1982**, *11–12*, 768–773. [[CrossRef](#)]
118. Dixon, R.A.; Williams, J.J.; Morris, D.; Rebane, J.; Jones, F.H.; Egdell, R.G.; Downes, S.W. Electronic states at oxygen deficient $WO_3(001)$ surfaces: A study by resonant photoemission. *Surf. Sci.* **1998**, *399*, 199–211. [[CrossRef](#)]
119. Bussolotti, F.; Lozzi, L.; Passacantando, M.; La Rosa, S.; Santucci, S.; Ottaviano, L. Surface electronic properties of polycrystalline WO_3 thin films: A study by core level and valence band photoemission. *Surf. Sci.* **2003**, *538*, 113–123. [[CrossRef](#)]
120. Jones, F.H.; Rawlings, K.; Foord, J.S.; Egdell, R.G.; Pethica, J.B.; Wanklyn, B.M.R.; Parker, S.C.; Oliver, P.M. An STM study of surface structures on $WO_3(001)$. *Surf. Sci.* **1996**, *359*, 107–121. [[CrossRef](#)]
121. Karazhanov, S.Z.; Zhang, Y.; Wang, L.W.; Mascarenhas, A.; Deb, S. Resonant defect states and strong lattice relaxation of oxygen vacancies in WO_3 . *Phys. Rev. B* **2003**, *68*, 233204. [[CrossRef](#)]
122. Karazhanov, S.Z.; Zhang, Y.; Mascarenhas, A.; Deb, S.; Wang, L.W. Oxygen vacancy in cubic WO_3 studied by first-principles pseudopotential calculation. *Solid State Ion.* **2003**, *165*, 43–49. [[CrossRef](#)]
123. Chatten, R.; Chadwick, A.V.; Rougier, A.; Lindan, P.J.D. The oxygen vacancy in crystal phases of WO_3 . *J. Phys. Chem. B* **2005**, *109*, 3146–3156. [[CrossRef](#)] [[PubMed](#)]
124. Deb, S.K. Opportunities and challenges in science and technology of WO_3 for electrochromic and related applications. *Sol. Energy Mater. Sol. Cells* **2008**, *92*, 245–258. [[CrossRef](#)]

125. Lambert-Mauriat, C.; Oison, V. Density-functional study of oxygen vacancies in monoclinic tungsten oxide. *J. Phys. Condens. Matter* **2006**, *18*, 7361–7371. [[CrossRef](#)]
126. Wang, F.; Di Valentin, C.; Pacchioni, G. Semiconductor-to-metal transition in WO_{3-x} : Nature of the oxygen vacancy. *Phys. Rev. B* **2011**, *84*, 073103. [[CrossRef](#)]
127. Gerosa, M.; Di Valentin, C.; Onida, G.; Bottani, C.E.; Pacchioni, G. Anisotropic Effects of Oxygen Vacancies on Electrochromic Properties and Conductivity of γ -Monoclinic WO_3 . *J. Phys. Chem. C* **2016**, *120*, 11716–11726. [[CrossRef](#)]
128. Mehmood, F.; Pachter, R.; Murphy, N.R.; Johnson, W.E.; Ramana, C.V. Effect of oxygen vacancies on the electronic and optical properties of tungsten oxide from first principles calculations. *J. Appl. Phys.* **2016**, *120*, 233105. [[CrossRef](#)]
129. Migas, D.B.; Shaposhnikov, V.L.; Rodin, V.N.; Borisenko, V.E. Tungsten oxides. I. Effects of oxygen vacancies and doping on electronic and optical properties of different phases of WO_3 . *J. Appl. Phys.* **2010**, *108*, 093713. [[CrossRef](#)]
130. Lambert-Mauriat, C.; Oison, V.; Saadi, L.; Aguir, K. Ab initio study of oxygen point defects on tungsten trioxide surface. *Surf. Sci.* **2012**, *606*, 40–45. [[CrossRef](#)]
131. Ping, Y.; Goddard, W.A.; Galli, G.A. Energetics and Solvation Effects at the Photoanode/Catalyst Interface: Ohmic Contact versus Schottky Barrier. *J. Am. Chem. Soc.* **2015**, *137*, 5264–5267. [[CrossRef](#)] [[PubMed](#)]
132. Albanese, E.; Di Valentin, C.; Pacchioni, G. H_2O Adsorption on WO_3 and WO_{3-x} (001) Surfaces. *ACS Appl. Mater. Interfaces* **2017**, *9*, 23212–23221. [[CrossRef](#)]
133. Haber, J.; Janas, J.; Schiavello, M.; Tilley, R.J.D. Tungsten oxides as catalysts in selective oxidation. *J. Catal.* **1983**, *82*, 395–403. [[CrossRef](#)]
134. Monter-Guzmán, J.Y.M.; Chu, X.; Comini, E.; Epifani, M.; Zanella, R. How Chemoresistive Sensors Can Learn from Heterogeneous Catalysis. Hints, Issues, and Perspectives. *Chemosensors* **2021**, *9*, 193. [[CrossRef](#)]
135. Ramis, G.; Cristiani, C.; Elmi, A.S.; Villa, P.; Busca, G. Characterization of the Surface-Properties of Polycrystalline WO_3 . *J. Mol. Catal.* **1990**, *61*, 319–331. [[CrossRef](#)]
136. Kanan, S.M.; Lu, Z.X.; Cox, J.K.; Bernhardt, G.; Tripp, C.P. Identification of surface sites on monoclinic WO_3 powders by infrared spectroscopy. *Langmuir* **2002**, *18*, 1707–1712. [[CrossRef](#)]
137. Ma, S.; Amar, F.G.; Frederick, B.G. Surface Heterogeneity and Diffusion in the Desorption of Methanol from $\text{WO}_3(001)$ Surfaces. *J. Phys. Chem. A* **2003**, *107*, 1413–1423. [[CrossRef](#)]
138. Ma, S.; Frederick, B.G. Reactions of aliphatic alcohols on $\text{WO}_3(001)$ surfaces. *J. Phys. Chem. B* **2003**, *107*, 11960–11969. [[CrossRef](#)]
139. Ling, S.; Mei, D.; Gutowski, M. Reactivity of hydrogen and methanol on (001) surfaces of WO_3 , ReO_3 , WO_3/ReO_3 and ReO_3/WO_3 . *Catal. Today* **2011**, *165*, 41–48. [[CrossRef](#)]
140. Ge, Q.F.; Gutowski, M. A Comparative Study of Methanol Adsorption and Dissociation over $\text{WO}_3(001)$ and $\text{ReO}_3(001)$. *Top. Catal.* **2015**, *58*, 655–664. [[CrossRef](#)]
141. Wang, F.G.; Di Valentin, C.; Pacchioni, G. DFT Study of Hydrogen Adsorption On the Monoclinic WO_3 (001) Surface. *J. Phys. Chem. C* **2012**, *116*, 10672–10679. [[CrossRef](#)]
142. Zhang, L.; Wen, B.; Zhu, Y.-N.; Chai, Z.; Chen, X.; Chen, M. First-principles calculations of water adsorption on perfect and defect $\text{WO}_3(001)$. *Comput. Mater. Sci.* **2018**, *150*, 484–490. [[CrossRef](#)]
143. Hurtado-Aular, O.; Vidal, A.B.; Sierraalta, A.; Anez, R. Periodic DFT study of water adsorption on m- $\text{WO}_3(001)$, m- $\text{WO}_3(100)$, h- $\text{WO}_3(001)$ and h- $\text{WO}_3(100)$. Role of hydroxyl groups on the stability of polar. *Surf. Sci.* **2020**, *694*, 121558. [[CrossRef](#)]
144. Hubner, M.; Simion, C.E.; Haensch, A.; Barsan, N.; Weimar, U. CO sensing mechanism with WO_3 based gas sensors. *Sens. Actuators B Chem.* **2010**, *151*, 103–106. [[CrossRef](#)]
145. Staerz, A.; Berthold, C.; Russ, T.; Wicker, S.; Weimar, U.; Barsan, N. The oxidizing effect of humidity on WO_3 based sensors. *Sens. Actuators B Chem.* **2016**, *237*, 54–58. [[CrossRef](#)]
146. Kohl, D. Surface processes in the detection of reducing gases with SnO_2 -based devices. *Sens. Actuators* **1989**, *18*, 71–113. [[CrossRef](#)]
147. Pokhrel, S.; Simion, C.E.; Teodorescu, V.S.; Barsan, N.; Weimar, U. Synthesis, Mechanism, and Gas-Sensing Application of Surfactant Tailored Tungsten Oxide Nanostructures. *Adv. Funct. Mater.* **2009**, *19*, 1767–1774. [[CrossRef](#)]
148. Staerz, A.; Kobald, A.; Russ, T.; Weimar, U.; Hemeryck, A.; Barsan, N. Thermal Water Splitting on the WO_3 Surface: Experimental Proof. *ACS Appl. Electron. Mater.* **2020**, *2*, 3254–3262. [[CrossRef](#)]
149. Staerz, A.; Somacescu, S.; Epifani, M.; Kida, T.; Weimar, U.; Barsan, N. WO_3 -Based Gas Sensors: Identifying Inherent Qualities and Understanding the Sensing Mechanism. *ACS Sens.* **2020**, *5*, 1624–1633. [[CrossRef](#)]
150. Oison, V.; Saadi, L.; Lambert-Mauriat, C.; Hayn, R. Mechanism of CO and O_3 sensing on WO_3 surfaces: First principle study. *Sens. Actuators B Chem.* **2011**, *160*, 505–510. [[CrossRef](#)]
151. Saadi, L.; Lambert-Mauriat, C.; Oison, V.; Ouali, H.; Hayn, R. Mechanism of NO_x sensing on WO_3 surface: First principle calculations. *Appl. Surf. Sci.* **2014**, *293*, 76–79. [[CrossRef](#)]
152. Ye, K.; Li, K.; Lu, Y.; Guo, Z.; Ni, N.; Liu, H.; Huang, Y.; Ji, H.; Wang, P. An overview of advanced methods for the characterization of oxygen vacancies in materials. *TrAC Trends Anal. Chem.* **2019**, *116*, 102–108. [[CrossRef](#)]